Engineering and Technology Journal
Journal homepage: https://etj.uotechnology.edu.iq

Improving the charging rate and energy recovery of triplex tube heat storage-based pcm with mono/hybrid nanoparticles

Ibrahim E. Sadiq*, Sattar Aljabair, Abdulhassan A. Karamallah

Mechanical Engineering Dept., University of Technology-Iraq, Alsina'a street, 10066 Baghdad, Iraq.
*Corresponding author Email: me.19.27@grad.uotechnology.edu.iq

HIGHLIGHTS

- The heat transfer performance of energy storage was improved.
- Hybrid nano-PCM was the most efficient enhancer.
- An optimal 1.6% volume fraction balanced performance and economics.
- 1.6% hybrid nano-PCM reduced overall melting time by 16.8%.

ARTICLE INFO

Handling editor: Jalal M. Jalil

Keywords:
Triplex tube heat storage
Heat transfer
Phase change material
Melting process
Nano-PCM

ABSTRACT

Latent thermal energy storage systems are widely utilized to match the inequality between heat supply and demand. Despite these systems' wide range of uses in various applications, their high potential is limited by the slow charging rate. The target of this study is to augment the thermal performance of paraffin-based on triplex tube heat storage by dispersion of two different types of conductive mono nanoparticles (Al_2O_3, CuO) and hybrid Nano additives of various volume fractions (0.4, 0.8, 1.6, 3.2%) into paraffin wax. The experimental work involves measurements and preparation of the considered Nano-PCM. The enthalpy porosity model and finite volume method simulated the melting process. The study also investigated the temperature and liquid fraction variations in the axial, radial, and angular directions throughout melting to aid in predicting heat transfer in the storage throughout the phase transition process of PCM. Results revealed that including 1.6% of hybrid nanoparticles in PCM can increase the stored energy by 5.97%. The results also indicated that the hybrid nano-PCM exhibits the best phase transition rate and energy recovery for all volume fractions compared to mono-nano-PCM. At 1.6% volume fraction, the storage efficiency can be improved up to 76.8%, 75.5%, and 73.63% for hybrid nano-PCM, Al_2O_3-PCM, and CuO-PCM, respectively.

1. Introduction

The importance of sustainable energy and waste heat recovery from factories is growing to overcome the energy shortage issue and environmental crisis. However, waste heat in traditional factories and sustainable energy sources (e.g., wind and solar power) exhibits periodic and intermittent patterns. Therefore, utilizing thermal storage devices is crucial for maintaining the efficiency and stability of these energy sources.

Thermal storage devices can be categorized into three types according to their working substance: sensible heat storage, thermochemical heat storage, and latent heat storage [1,2]. The latent heat thermal energy storage device is favorable because it has a greater heat storage capacity than the sensible heat storage device [3,4]. Moreover, the phase change material (PCM), which serves as the working substance of latent heat energy storage devices, shows insignificant variation in its chemical and thermal characteristics even after conducting numerous thermal cycles.

Storage unit-based PCM has been effectively incorporated into various applications, including solar thermal energy, waste heat recovery, building energy conservation, and electronics cooling. However, the low thermal conductivity of PCM causes a slow rate of charging and discharging process, which affects the overall performance of the system. Therefore, to resolve this problem, several techniques have been developed over the last few decades. These enhancement techniques involve using fins [5,6], heat pipes [7,8], highly conductive metal foam [9,10], nanoparticles [11,12], graphite composites [13,14], and carbon nanotubes [15,16].

Al-Abidi et al. [17] examined the influence of longitudinal fin arrangement on the charging time of PCM in triplex tube heat storage (TTHS). Several fins arrangements (internal, external, and internal-external) and variations in fin length and fin thickness were experimentally and numerically investigated. According to the result, the optimal case's total charging time was reduced to

http://doi.org/10.30684/etj.2023.144438.1631
Received 06 November 2023; Received in revised form 18 November 2023; Accepted 22 December 2023; Available online 06 January 2024
2412-0758/University of Technology-Iraq, Baghdad, Iraq

34.7%. The numerical study of the phase transition process in a vertical PCM container of double tubes coupled with sinusoidal wavy fins was carried out by Shahsavar et al., [18]. Different wavelengths and wave amplitudes for these fins were examined to determine the most efficient configuration. Their result revealed that the most effective values for these fin parameters were identified as 1 and 2 mm, respectively. These values enhance the phase transition rate by around 43.5% compared to the case with no fin.

Baou et al. [19] employed metal and graphite foams to augment the thermal performance of a car radiator. To achieve that, various obstacle and porous media configurations were examined. It was discovered that there was a 237% improvement in the overall thermal performance of the system by choosing the optimal design and material of porous foam. The phase transition characteristics of the n-octadecane PCM in a cavity partially occupied with copper metal foams was studied by Liu et al., [20]. It utilized four configurations of partial porous filling with different metal foam filling techniques to discover the most effective one. The experimental findings showed that although metal foams enhance thermal conduction, they also diminish the cavity's convection current.

Moreover, the best outcomes occur when the lower porous filling is used. Abbasi et al. [21] evaluated the effect of porous media for enhancing the charging process in shell and tube heat storage based PCM. Melting front (solid liquid interface) and the liquid fraction distribution were observed and investigated. Their result showed that total charging time can be reduced to 80% by decreasing the foam porosity. Methods such as porous media or fins are superior in accelerating heat transition rate. However, they decrease the amount of PCM in the storage and consequently lead to a decrease in the overall thermal storage capacity of the unit. Including highly conductive nano-scale powder into PCMs to enhance their thermal characteristics may be more efficient in terms of PCM volume utilization.

Nanoparticles are granular matter with sizes ranging from 1 to 100 nanometers. They are extensively utilized in many applications, such as photocatalysis, polymer reinforcing, and heat transfer enhancement. Many studies have focused on using nanoparticles to enhance the thermal characteristics of fluids [22]. Hamali and Almusawa [23] applied the Galerkin technique to investigate water freezing with the assistance of extended surfaces and nanoparticles using a two-dimensional model. It utilized Y-shaped fins and CuO nanoparticles. Based on the result, including these nanoparticles can accelerate the freezing process by approximately 10%. Likewise, Rothan et al. [24] studied the effect of CuO nanopowder's shape factor on PCM's discharging process in the presence of radial fins. It was found that a larger shape factor results in a shorter discharging time. Quantitatively, around 10% of the improvement was achieved by distributing CuO nanoparticles with the optimum shape factor. The utilization of nanoparticles to speed up the paraffin charging process in a large-scale shell and tube thermal energy storage was conducted by Chiban et al., [25]. Four distinct types of nanoparticles were evaluated within this PCM by using a two-dimensional computational model.

Additionally, the different volume concentrations of these nanoparticles were analyzed. It was concluded that despite the inclusion of nanoparticles being effective on the charging rate, boosting their volume concentration does not cause a significant impact on the values of liquid fraction and temperature. Zhang et al. [26] conducted studies to investigate molten salt flow's thermal characteristics using silicon dioxide nanoparticles in a concentrating solar power plant. The experimental result showed that the existence of these nanoparticles leads to an approximately 11.5% increase in the Nusselt number. In addition, several correlations were proposed to determine the thermal properties of flowing molten salt. Ghalambaz et al. [27] applied the Galerkin finite element approach to investigate improving the charging process in a cavity occupied with PCM. They examined the use of both mono and hybrid nanoparticles. The lateral sides of the chamber were thermally insulated, while the bottom and top surfaces were maintained at constant temperatures. They deduced that the presence of nanoparticles significantly influences the melting front at high Fourier numbers. Ghalambaz et al. [28], in another paper, conducted a study to assess the melting flow of paraffin in a cavity with the presence of a magnetic field. The thermal boundary conditions of the cavity were identical to those in their last investigation, with the addition of an external line-source magnet to generate a magnetic field. They found that the magnetic field's effect is insignificant at the beginning of the charging process, but it becomes increasingly considerable as time progresses. Sadiq et al. [29] carried out an experimental and numerical study to discover the thermal performance of a triplex tube heat storage by inserting paraffin wax on the annulus side. A blend of Al_2O_3 and CuO was used as conductive particle to enhance the thermal characteristics of Paraffin. It was observed that adding 3.2% of hybrid nanoparticles can decrease total melting time by 18.6%. Afsharpanah et al. [30] performed a comparison of different carbon-based nanoparticles in cold energy storage system for air cooling purposes in buildings. Additives of graphene nanoparticles and single-walled and multi-walled carbon nanotubes (SWCNT and MWCNT) were evaluated in this unit in comparison to metal-oxide nanoparticles in an effort to increase the discharging rate. Among these types of nanoparticles, it was discovered that the MWCNT nanoparticles exhibited the most favorable result, with a freezing rate that was up to 70.1% faster than the basic model. Arıcı et al. [31] used a combination of CuO nanoparticles and internal fins to accelerate the phase transition process of a PCM with temperature-dependent characteristics. A variety of orientations of cooled/heated surfaces were examined, in addition to fins of varying shapes and dimensions that were mounted to these surfaces. The obtained result showed that the charging rate can be improved by about 68% compared to the case with no fins if the optimal fin shape is chosen and placed correctly.

According to the previous survey, several methods for enhancing heat transfer involve using extended surfaces, porous materials, multiple PCMs, and conductive nanopowder in PCM. It was observed that fins and porous materials are widely utilized in the literature due to their ease of design and low cost. However, the existence of fins or metal foam in PCM may resist the growth of the natural current induced in the molten Region, which in turn would minimize the positive impact of extended surfaces on the thermal performance of storage. Furthermore, integrating solid material (e.g., fins and porous matrix) reduces the amount of PCM. It increases the overall storage weight, which deteriorates total storage energy and influences the mobility of these units. On the other hand, changing the configuration of heat storage is difficult to manufacture and does not always enhance the thermal performance of storage. Another candidate is to boost the thermal conductance of PCM by incorporating highly

conductive nanoscale powder, which has been shown to be suitable and easy to achieve with relatively little increase in overall storage weight.

In this paper, the influence of using various types of nanoparticles with the PCM on triplex tube energy storage (TTHS) performance is numerically and experimentally performed. Paraffin wax as PCM is positioned in an annulus space between the intermediate and inner tubes, whereas heat transfer fluid (HTF) passes through both the inner tube and outer annulus. The originality of this work is to investigate the melting process of three different storage substances, including Al_2O_3-PCM, CuO-PCM, and (Al_2O_3+ CuO)-PCM and compare with pure PCM. To find out the best substance with the optimal volume fraction of nanoparticles, three samples are prepared by inclusion of 0.4%, 0.8%, 1.6%, and 3.2% by volume of nanoparticles, respectively, in paraffin, for each type of nanoparticles. The literature showed a shortage of studies concerning the phase change characteristic of mono and hybrid-nano PCM in TTHS. Therefore, the major objective of this research is to discover the influence of mono and hybrid nanoparticle dispersion on heat transfer behavior throughout PCM melting in TTHS. Besides that, the variation of average temperature in the axial, radial, and angular directions is analyzed to assess the thermal response along the three directions. These averages were computed using thermocouple readings from various positions of the thermal storage facility.

2. Experimental test and procedure

2.1 Experimental apparatus

The thermal storage device is triplex tube heat storage with 7 kg of PCM between the inner and middle tubes. A photograph and schematic diagram of the testing apparatus utilized in this investigation are depicted in Figure 1 and Figure 2, respectively. Apparently, HTF undergoes two cycles: the hot water cycle, during which thermal energy is transferred from heated water to PCM, and the warm-water cycle, where absorbed energy by PCM is transferred back into warm water. The test section comprises three horizontally arranged concentric tubes 600 mm long, see Figure. The diameters of the inner tube, middle tube, and outer tube are 50 mm, 150 mm, and 200 mm, respectively. The inner and middle tubes are made of copper to reduce thermal resistance. A carbon steel tube is chosen for the outer tube. Two circular carbon steel flanges were provided to close both ends of the storage unit. Each flange has a central hole of 53 mm diameter to allow passage of the inner tube. Each flange is drilled with a 10 mm diameter hole to facilitate the passage of thermocouple wires. A 50 mm thick thermal insulator made of glass wool, with a thermal conductivity of 0.04 W/mK, wraps around the storage device to reduce heat loss.

To quantify the temperature variation of PCM, sixty thermocouples of K-type were fastened within PCM and uniformly placed along the axial axis (sections A, B, and C), as illustrated in Figure 3. Twenty thermocouples are arranged in a radial and angular orientation over each section, as seen in Figure 4. In addition, one thermocouple is installed at the inlet to record the temperature of the inlet water, and two thermocouples at the outlet to record the temperature of the outlet water. One is on the tube side, while the other is on the outer annulus. All thermocouples, which had a temperature measuring scope of 0–200°C and an accuracy of ±0.3°C, were connected to a data logger. The data logger was then connected to a computer. In addition, a rotameter with a precision of 4% was employed to quantify the flow rate of HTF.

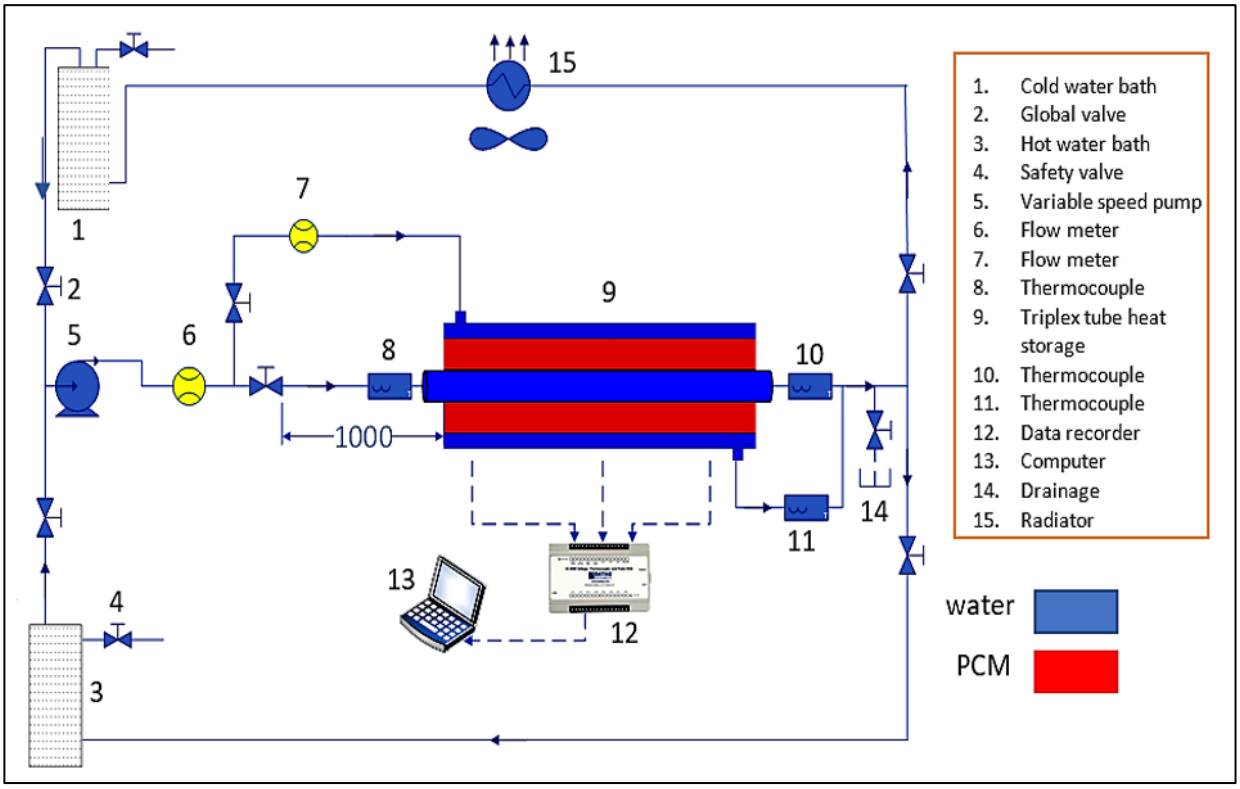

Figure 1: Schematic drawing of test rig

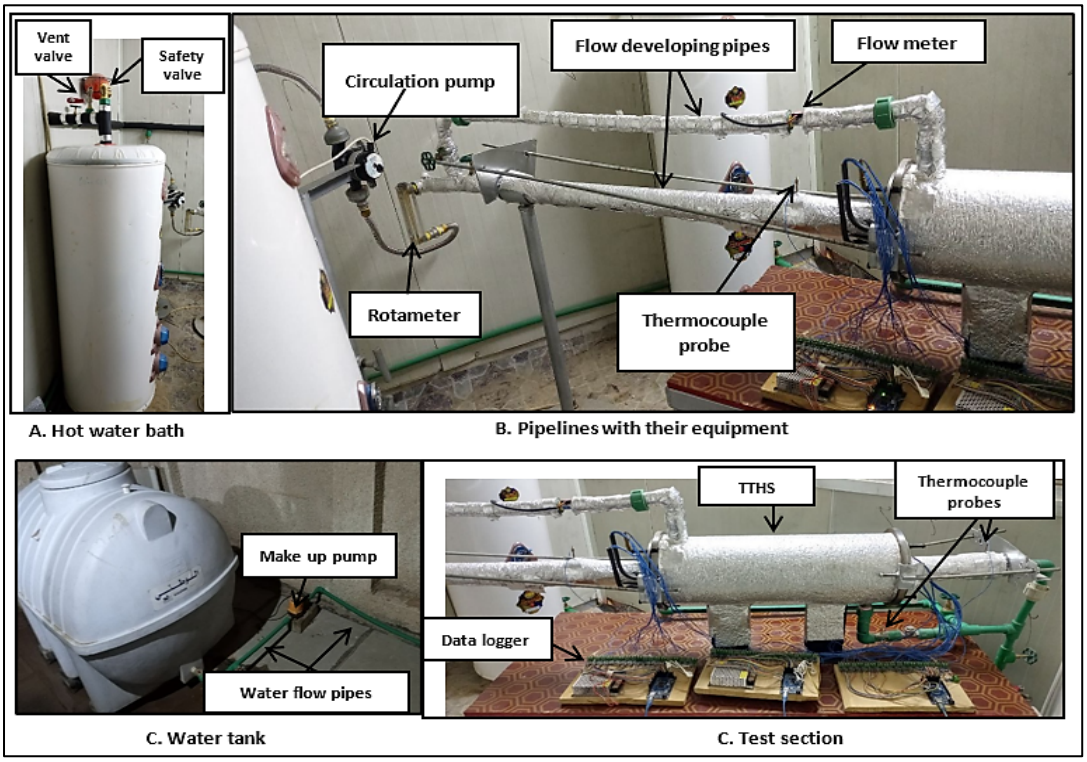

Figure 2: Photo of test rig parts

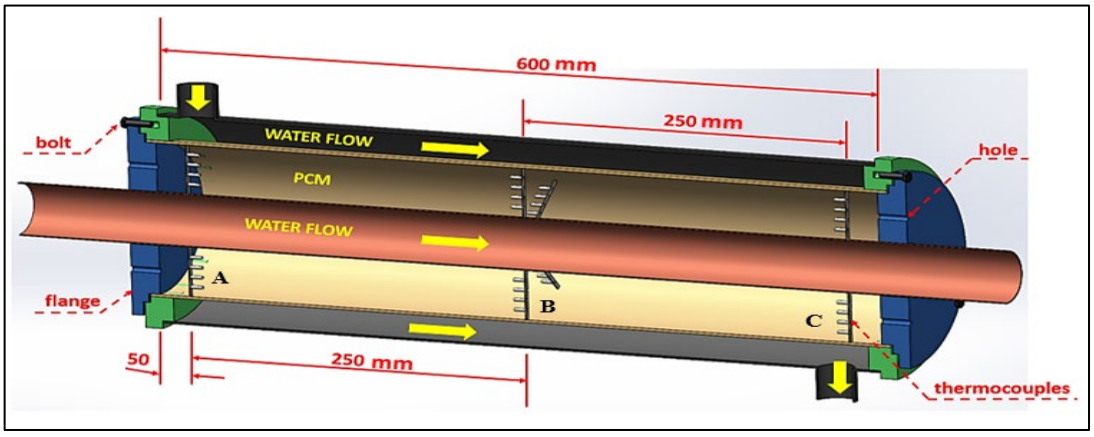

Figure 3: Sectional sketch of triplex tube heat storage

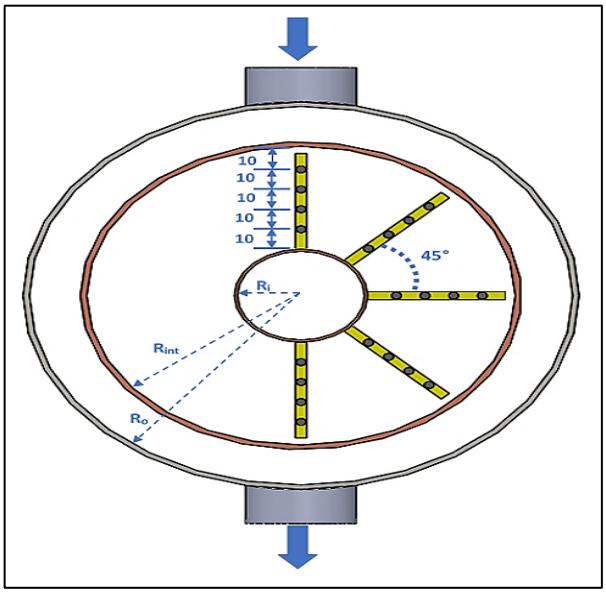

Figure 4: Schematic drawing of thermocouple locations

2.2 Experimental procedure

The water reservoir of 250 liters is equipped with a thermoelectric heater of 1500 W and a thermostat to heat the water and maintain constant water temperature throughout the experiment. Prior to the commencement of each test, warm water at a temperature of 30°C is circulated from the warm water reservoir into the inner tube and outer annulus of the TTHS to achieve a constant initial thermal condition. This process proceeded until PCM temperature (thermocouples readings) approached the water inlet temperature, which may last about 1 hour. The experiment began by delivering hot water at a pre-determined flow rate from the water reservoir with a steady temperature to the TTHS, where the PCM gains heat from the water. The data-collecting device recorded temperature values from thermocouples every 1-minute. However, the test was ended as the entire PCM became in a liquid state. This can be observed when all temperature measurements from the thermocouples become higher than the melting temperature, and the discrepancy between the inlet and outlet temperatures of the HTF decreases to 0.5°C. This implies that PCM absorbs as much energy as possible, and the system approaches thermal equilibrium, which may require 3–3.5 hours, according to the case.

2.3 PCM selections

Paraffin wax, supplied by a paraffin corporation in China, was used as the PCM in this study. Literature frequently employs paraffin due to its chemical stability during the charging cycle, high latent heat of fusion, and non-toxicity compared to hydrated ions and non-organic paraffin. Differential scanning calorimetry (DSC) test was conducted to find out the paraffin's specific heat, latent heat of fusion, and phase transition temperature range. An experiment was undertaken on a 14.6-gram sample of PCM, with the temperature ranging from 40°C to 900°C and a heating rate of 20°C /min. Figure 5 displays the DSC thermogram of the paraffin. The latent heat of fusion can be obtained by applying numerical integration to the area under the curve. The phase transition range can be determined by identifying the onset point and the point corresponding to the curve's peak. Table 1 presents the results acquired from this test.

2.4 Preparation of nanoparticles dispersed paraffin

The hybrid nano-additives were created by carefully blending equal Al_2O_3 and CuO nanoparticles in a clean container. Various hybrid nano volume fractions (0.4%, 0.8%, 1.6%, and 3.2%) were distributed within the molten paraffin. The choice of these volume concentrations is according to prior literature, which recommended a low-volume fraction of nanoparticles due to the adverse effects of a high-volume fraction. These effects include particle agglomeration, diminishing latent heat, and increased material cost [32,33].

To make nano-PCM, PCM is initially heated in a boiling water bath. Afterward, the nanoparticles were dispersed gradually into the molten PCM. The compound was heated and stirred simultaneously in the mechanical blender for 30 minutes to get a homogeneous compound. Subsequently, the mixture was poured layer by layer into the annulus to avoid forming any air pockets in the paraffin. A sufficient duration was allocated to solidify each liquid layer, after which the subsequent liquid layer was poured into storage. The process was repeated until the annulus was filled with paraffin. All the preparation processes are clearly outlined and depicted in Figure 6.

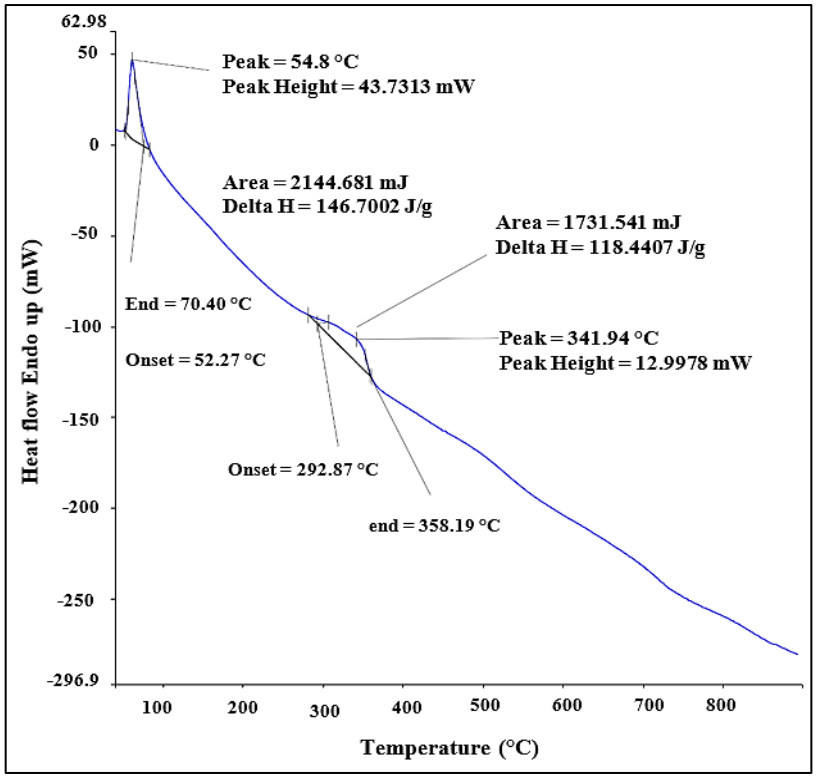

Figure 5: Heat transfer variation vs temperature for tested paraffin wax

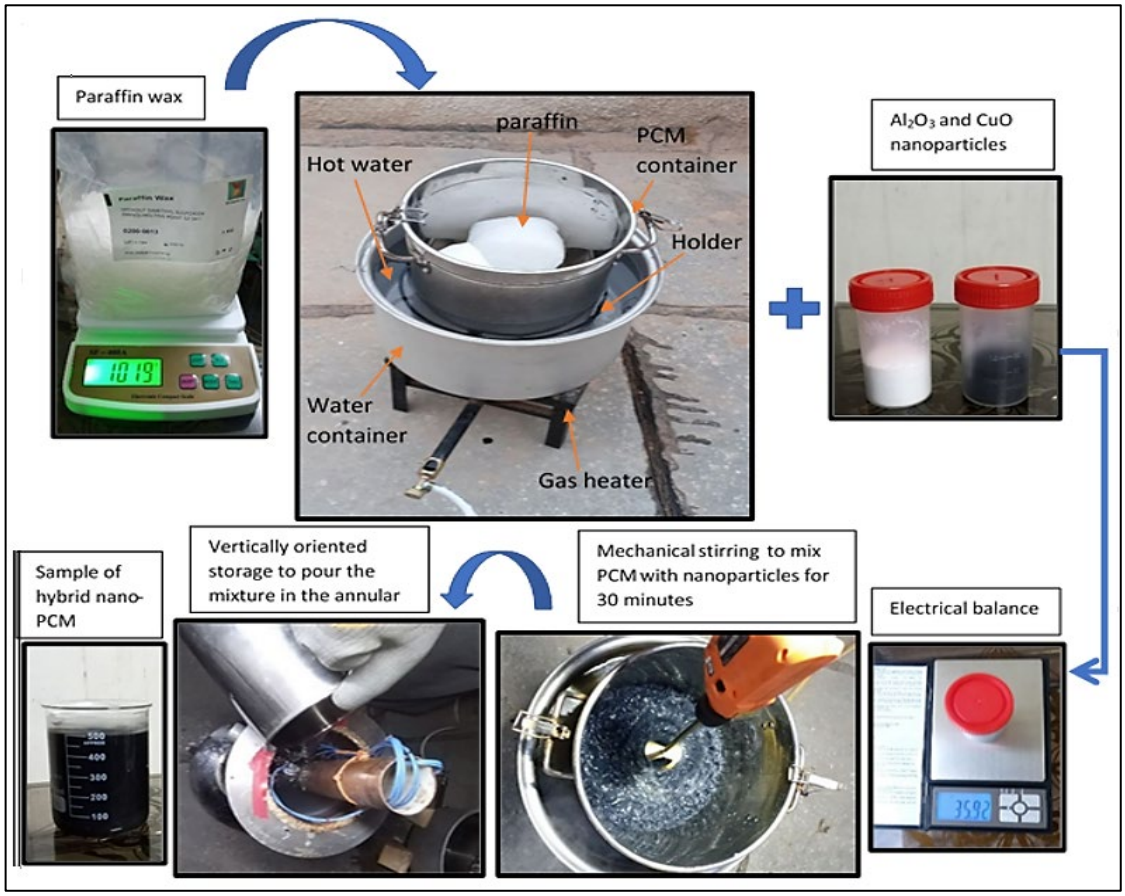

Figure 6: Heat transfer variation vs temperature for tested paraffin wax

2.5 XRD and TEM analysis of nanoparticles

Structural analysis of Al_2O_3 and CuO nanoparticles was carried out using X-ray diffraction (XRD). This analysis used a Bruker AXS D8 Advance X-ray diffractometer, employing Cu-Kα radiation within the 15–70° range and a step increment of 0.02° degrees. The grain size was determined by applying the Scherrer formula described by Fathi and Hanifi [34], as expressed in Equation 1. In this equation, the sample's average crystallite size (D) is related to the broadening of its diffraction peaks (β). In contrast, λ is the wavelength of radiation, θ is the Bragg angle, and K is a fixed value of 0.9. On the other hand, the framework of nanoparticles in the PCM was identified and the data from the XRD analysis was verified using a transmission electron microscope (TEM) imaging devices for morphological evaluation.

$$D = \frac{K\,\lambda}{(\beta)\cos\theta} \tag{1}$$

2.6 Data reduction

The amount of stored energy and thermal storage efficiency can be theoretically computed using the relations presented in Table 1.

Table 1: Energy equations and theoretical efficiency

Variables	Equations
Heat transfer rate in tube side	$q_t = \frac{1}{2}\left(\dot{m}c_{p,HTF}\left(T_{\text{in}} - T_{\text{out,t}}\right)\right)$
Heat transfer rate in shell side	$q_s = \frac{1}{2}\left(\dot{m}c_{p,HTF}\left(T_{\text{in}} - T_{\text{out,s}}\right)\right)$
Total Heat transfer rate	$q_{total} = q_t + q_s$
Accumulative energy [35]	$Q_{\text{charging}} = \sum_0^t q_{total}\Delta t$
Maximum heat storage	$Q_{\max} = M_{PCM}[c_{P,PCM}(T_{\text{solidus}} - T_{\text{ini}}) + (L) + c_{P,PCM}(T_{\text{end}} - T_{\text{liquidus}})]$
Thermal storage efficiency [36]	$n_{\text{theory}} = \frac{Q_{\text{charging}}}{Q_{max}}$

2.7 Uncertainty analysis

Because of measurement device errors, uncertainty analysis is required. The analysis was performed based on Moffat [37]. The total uncertainty of heat transfer for different volume fractions is presented in Table 2.

(R) is estimated as follows:

$$\delta RX_i = \frac{\partial R}{\partial X_i} * \delta X_i \tag{2}$$

$$S_R = \left[\sum_{i=1}^{m} (\frac{\partial R}{\partial X_i} * \delta X_i)^2\right]^{0.5} \tag{3}$$

S_R is the uncertainty in the result, which can be expressed in Equation 4:

$$S_R = \left[(\frac{\partial R}{\partial \dot{X}_1} S_{X1})^2 + (\frac{\partial R}{\partial \dot{X}_2} S_{X2})^2 + \cdots \ldots \ldots + (\frac{\partial R}{\partial \dot{X}_i} S_{Xi})^2\right]^{0.5} \tag{4}$$

The heat transfer (Q) is a function of two variables:

$$Q = f(\dot{m}, \Delta T) \tag{5}$$

$$\frac{\partial Q}{\partial \dot{m}} = C_p \Delta T \tag{6}$$

$$\Delta T = T_{in} - T_{out} \tag{7}$$

$$\frac{\partial Q}{\partial \Delta T} = \dot{m} C_p \tag{8}$$

The uncertainty of the heat transfer (S_Q) is given in Equation 9 as follows:

$$S_Q = \left[\left(\frac{\partial Q}{\partial \dot{m}} S_{\dot{m}}\right)^2 + \left(\frac{\partial Q}{\partial \Delta T} S_{\Delta T}\right)^2\right]^{1/2} \tag{9}$$

$$Relative\ uncertainty = \frac{S_Q}{Q} \tag{10}$$

Table 2: Uncertainty for hybrid nano-PCM

Volume fraction (%)	Uncertainty (w)	Relative uncertainty (%)
0.4	7.896	2.039
0.8	5.177	1.077
1.6	4.194	0.777
3.2	3.761	0.640

3. Numerical model

3.1 Governing equations

The phase transition process in a TTHS is simulated utilizing the enthalpy porosity technique for three-dimensional models [38]. The subsequent assumptions are taken into consideration in the mathematical model:

- The flow regime is assumed to be laminar.
- The term of viscous dissipation has been neglected. Thus, the viscous incompressible flow are described by Navier-Stokes and thermal energy equations, respectively [39].
- The variation of HTF temperature and heat transfer with the surroundings are negligible.
- There is no-slip condition for fluid at the walls.
- Thermophysical properties of the PCM are temperature-dependent, excluding the specific heat, which is considered constant.

Based on the previous assumptions, the governing equations can be formulated as following:
Continuity equation:

$$\frac{\partial \rho_{\text{hnpcm}}}{\partial t} + \nabla \cdot \left(\rho_{\text{hnpcm}} \vec{V}\right) = 0 \tag{11}$$

Momentum equation:

$$\frac{\partial \vec{V}}{\partial t} + \vec{V} \cdot \nabla \vec{V} = \frac{1}{\rho_{\text{hnpcm}}} \left(-\nabla P + \mu_{hnPCM} \nabla^2 \vec{V} + (\rho\beta)_{hnPCM} \vec{g}\left(T - T_{ref}\right)\right) + \vec{S} \tag{12}$$

Thermal energy equation:

$$\frac{\partial h}{\partial t}+\frac{\partial(\nabla H)}{\partial t}+\nabla\cdot\left(\vec{V}h\right)=\nabla\cdot\left(\frac{k_{hnpcm}}{(\rho C_p)_{hnpcm}}\nabla H\right) \tag{13}$$

The enthalpy of the material can be estimated as the sum of the sensible enthalpy (h) and the latent heat (ΔH) [40]

$$H=h+\Delta H \tag{14}$$

where

$$h=h_{\text{ref}}+\int_{T_{\text{sef}}}^{T} C_p dT \tag{15}$$

The reference enthalpy (h_{ref}) is obtained at a reference temperature 273 K and Cp is the specific heat. The latent heat content can be written in terms of the latent heat of the material, *L*

$$\Delta H=\lambda L \tag{16}$$

where ΔH may vary from zero (solid) to *L* (liquid). Therefore, the liquid fraction, λ, can be defined from Equation 17:

$$\lambda=\begin{cases}\frac{\Delta H}{L}=0\ if\ T<T_{solidus}\\ \frac{\Delta H}{L}=1\ if\ T>T_{liquidus}\\ \frac{\Delta H}{L}=\frac{T-T_{solidus}}{T_{liquidus}-T_{solidus}}\ if\ T_{solidus}<T<T_{liquidus}\end{cases} \tag{17}$$

In Equation (12), $\vec{S}$ is Darcy's law damping terms (as source term) that is implemented to the momentum equation due to phase change effects on convective heat transfer, which is found as [41]:

$$\vec{\mathrm{S}}=\frac{(1-\lambda)^2}{\lambda^3}\mathrm{A_{mush}}\vec{\mathrm{V}} \tag{18}$$

The coefficient Amush is a mushy zone constant. This constant is large, usually 10^5–10^6 [42]. In the current study, Amush is assumed constant and assigned to 106. To model the paraffin's melting process in the existing Al_2O_3/CuO hybrid nanoparticles of different volume fraction, the subsequent relations were implemented to estimate the thermal characteristics of the hybrid nano-PCM.

The overall volume fraction of hybrid nanoparticles in the compound can be calculated from Equation19 [43]:

$$\varphi_{\mathrm{hnp}}=\varphi_{\mathrm{np1}}+\varphi_{\mathrm{np2}} \tag{19}$$

The density of mono nano-PCM can be predicted from Equation 20 [44, 45]:

$$\rho_{\mathrm{npcm}}=\rho_{\mathrm{np}}\varphi_{\mathrm{np}}+\left(1-\varphi_{\mathrm{np}}\right)\rho_{\mathrm{pcm}} \tag{20}$$

The density of hybrid nano-PCM (ρ_{hnpcm}) is presented in Equation 21:

$$\rho_{\mathrm{hnpcm}}=\rho_{\mathrm{hnp}}\varphi_{\mathrm{hnp}}+\left(1-\varphi_{\mathrm{hnp}}\right)\rho_{\mathrm{pcm}} \tag{21}$$

The subscript hnpcm represents a hybrid nano-PCM. ρ_{hnp} is the equivalent density of hybrid nanoparticles, which is presented in Equation (22) [43]:

$$\rho_{\mathrm{hnp}}=\frac{\varphi_{\mathrm{np1}}\rho_{\mathrm{np1}}+\varphi_{\mathrm{np2}}\rho_{\mathrm{np2}}}{\varphi_{\mathrm{hnp}}} \tag{22}$$

The following Equation (23) was utilized to theoretically calculate the value of the specific heat of mono nano-PCM, which is formulated according to the principle of mixture theory [44]:

$$\mathrm{C_{p,npcm}}=\frac{\mathrm{C_{p,np}}\,\rho_{\mathrm{np}}\,\varphi_{\mathrm{np}}+\mathrm{C_{p,pcm}}\,\rho_{\mathrm{pcm}}\,(1-\varphi_{\mathrm{np}})}{\rho_{\mathrm{npcm}}} \tag{23}$$

Specific heat of hybrid nano-PCM can be estimated from Equation 24:

$$C_{p,hnpcm} = \frac{C_{p,hnp}\ \rho_{hnp}\ \varphi_{hnp} + C_{p,pcm}\ \rho_{pcm}\ (1-\varphi_{hnp})}{\rho_{hnpcm}} \quad (24)$$

Equivalent specific heat ($C_{p,hnp}$) of hybrid nanoparticles can be calculated from Equation (25) [43]:

$$C_{p,hnp} = \frac{\varphi_{np1}\ C_{p.np1}\ \rho_{np1} + \varphi_{np2}\ C_{p,np2}\ \rho_{np2}}{\rho_{hnpcm}\ \varphi_{hnp}} \quad (25)$$

The viscosity of hybrid nano-PCM is estimated according to the Batchelor model [46] as presented in Equation 26:

$$\mu_{hnpcm} = \left(1 + 2.5\varphi_{hnp} + 6.2(\varphi_{hnp})^2\right)\mu_{pcm} \quad (26)$$

Maxwell's model was used to find the thermal conductivity of monospherical nanoparticles and well-mixed particles in a substance. It is derived according to the effective medium theory. The Equation (27) that Maxwell created can be used for low-volume fractions [47,48]:

$$k_{npcm} = \left(\frac{k_{np}+2k_{pcm}+2(k_{np}-k_{pcm})\varphi_{np}}{k_{np}+2k_{pcm}-(k_{np}-k_{pcm})\varphi_{np}}\right)k_{pcm} \quad (27)$$

The thermal conductivity of hybrid nano-PCM is obtained based on the Maxwell model in Equation 28:

$$k_{hnpcm} = \left(\frac{k_{hnp}+2k_{pcm}+2(k_{hnp}-k_{pcm})\varphi_{hnp}}{k_{hnp}+2k_{pcm}-(k_{hnp}-k_{pcm})\varphi_{hnp}}\right)k_{pcm} \quad (28)$$

Equivalent thermal conductivity of hybrid nanoparticles (k_{hnp}) is given in Equation 29 as [43]

$$k_{hnp} = \frac{(\varphi_{np1}\ k_{np1} + \varphi_{np2}\ k_{np2})}{\varphi_{hnp}} \quad (29)$$

Latent heat of fusion of mono nano-PCM is presented in Equation 30 [49]:

$$L_{hnpcm} = \frac{L_{pcm}\ \rho_{pcm}\left(1-\varphi_{np}\right)}{\rho_{nPCM}} \quad (30)$$

Latent heat of fusion of hybrid nano-PCM is presented in Equation 31 [50]:

$$L_{hnpcm} = \frac{L_{pcm}\ \rho_{pcm}\left(1-\varphi_{hnp}\right)}{\rho_{hnPCM}} \quad (31)$$

The thermophysical properties of paraffin, Al_2O_3, and CuO are listed in Table 3.

Table 3: Paraffin and nano-particle thermophysical properties [51,52]

Properties	Pure PCM	Al_2O_3	CuO
Density (kg/m3)	$\frac{750}{0.001(T-319.15)+1}$	3970 [53]	6500 [51]
Specific heat (J/kg °C)	2149	765 [51]	535.6 [51]
Thermal conductivity (w/m °C)	0.21 if $T < T_{solidus}$ 0.12 if $T > T_{liquidus}$	36 [52]	18 [52]
Viscosity (pa.s)	$0.001\exp\left(-4.25+\frac{1790}{T}\right)$	-	-
Latent heat of fusion (J/kg)	146700	-	-
Solidus temperature, °C	52	-	-
Liquidus temperature, °C	54	-	-
Thermal expansion factor (1/K)	0.001 [39]	-	-

3.2 Validation of numerical model

To validate the mathematical model, the time wise variation of average temperature of the PCM zone determined by the simulation is compared with the experimental result of Al-Abidi et al. [17] for an identical storage system as displayed in Figure 7. As can be seen, a maximum deviation of about 4.5%, can be noticed between the experimental and numerical results, indicating that the phase transition modeling is highly reliable and accurate. According to Reference [17], the storage dimensions and operating conditions for the verification process are outlined as follows:

- The inner, intermediate and outer tubes diameters of the storage device are 50.8, 150, and 200 mm, respectively.
- The initial temperature of the PCM was set to 27°C, whereas the HTF temperature was 90°C.
- The mass flow rate of the HTF was 8.3 l/min.
- The RT82 paraffin were used as PCM with solidus and liquidus temperature of 70°C and 82°C, respectively.

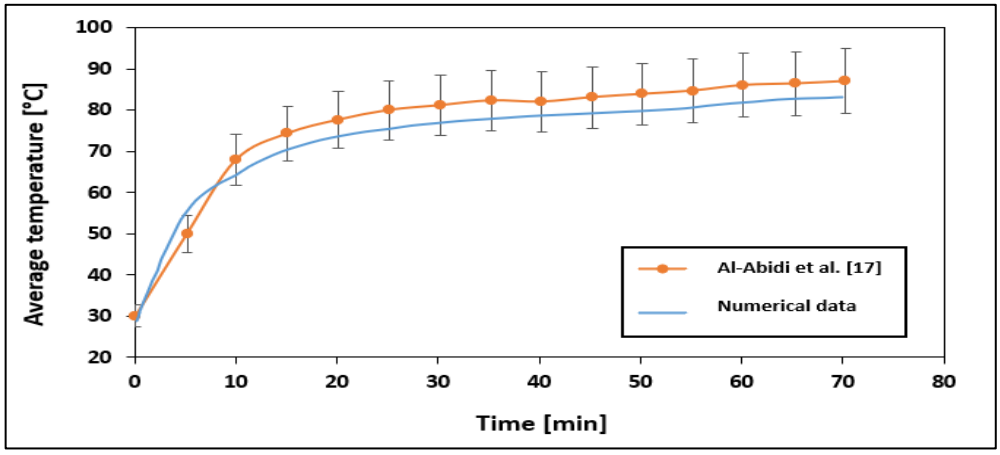

Figure 7: Comparison of the PCM average temperature of the present numerical data and experimental data provided [17]

3.3 Boundary and initial conditions

To guarantee that the entire phase change material (PCM) is initially in its solid state, the temperature at the beginning must be set at a value lower than the melting temperature. Therefore, the initial temperature was set to 30 c for all cases. The type "velocity-inlet" and "pressure-outlet" boundary conditions were selected for HTF at the inlet and outlet of the TTHS system, respectively. The mass flow rate of HTF was 3 kg/min, while HTF inlet temperature was 70°C. Since the outer surface of storage is insulated, the other tube surface in TTHS is chosen as an adiabatic wall. The computational domains with associated boundary conditions are demonstrated in Figure 8.

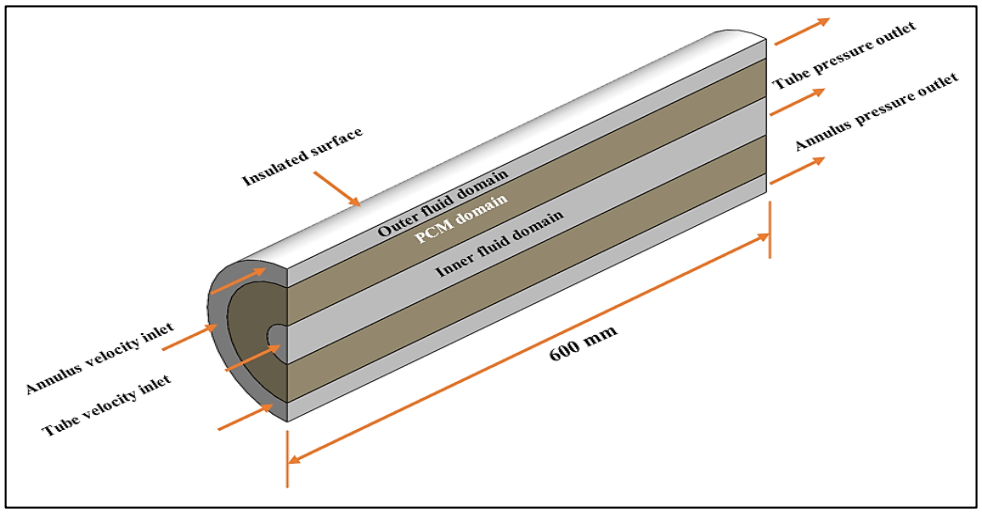

Figure 8: Physical domain and Boundary conditions of TTHS

3.4 Numerical schemes and validation

The group of partial differential equations was resolved using the ANSYS FLUENT 21 software. The QUICK differencing scheme [54] is utilized to solve the momentum and energy equations, while the PISO (Pressure Implicit with Splitting of Operator) algorithm [55] is employed for the pressure-velocity coupling. The PRESTO (Pressure Staggering Option) scheme was applied for pressure correction. The phase transition process of PCM is simulated using the enthalpy-porosity model [56], [57]. This mathematical model determines a liquid fraction for each computational cell according to the enthalpy balance.

To attain a stable solution via iterations, the under relaxation factors of 0.6, 0.3, 1, and 0.9 were applied, respectively, to the velocity components, pressure correction, thermal energy, and liquid fraction. The mesh independence test was accomplished by comparing the variations in total melting time over several grid sizes Table 4. It was found that the number of elements of 309120 was adequate to produce a solution independent of the number of elements. For each time step of 0.01 s, a total number of iterations of 20 was determined to be adequate in meeting the convergence criterion of 10-7 for the energy equation and 10-5 for the mass and momentum equations.

Table 4: Grid size and time step independence performed on a sample of nano-PCM

Case	Number of elements	Number of nodes	Time step (s)	Freezing time (s)	Relative error (%)
1	209670	218275	0.1	14731.54	5.83
2	307380	322595	0.1	14284.7	2.62
3	400530	415761	0.1	14120.45	1.44
4	307380	322595	0.01	13920	-
5	307380	322595	0.001	13844.83	0.54

To verify the present work, a comparison is performed between the experimental and numerical work of the present work. Figure 9 indicates the variation of the experimental and numerical average temperature for 0.4% volume fraction, 62°C HTF inlet temperature, and 3 kg/min mass flow rate. There is a good agreement between the experimental and numerical results with about a 4% average discrepancy.

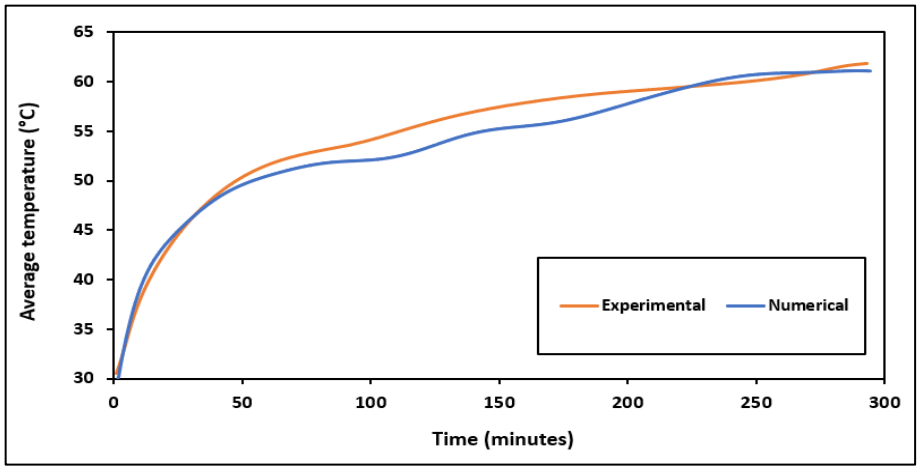

Figure 9: Comparison of average temperature between the experimental and numerical result

4. Results and discussion

4.1. Thermal variation for energy storage

Most experimental and numerical investigations have adopted a two-dimensional methodology to examine the thermal performance of energy storage. These studies typically analyze the PCM's behavior in radial and angular directions (R, θ) or the radial and axial directions (R, Z). This study analyzes the variation of average temperature in the axial, radial, and angular directions to assess the thermal response along the three directions. These averages were computed using thermocouple readings from various positions of the thermal storage facility.

4.1.1 Axial variation

Figures 10-12 depict the temporal variation of average temperature along the axial direction, 3-D temperature contour, and 3-D liquid-fraction contours. The average PCM temperatures were obtained by taking the average value of 20 thermocouple recordings located at various sections along the storage: section A (10 mm), section B (300 mm), and section C (590 mm). As can be seen from Figure 10, The highest average temperature can be noticed at section A, which is nearest to the inlet, followed by section B and then section C. This is because the heat transfer is the highest at section A, followed by sections B and C. These heat transfer variations are related to the fact that as HTF passes through the heat storage, it rejects heat to PCM. Therefore, the temperature of HTF and the temperature of tube surfaces decrease along the storage, and hence, the heat transfer rate decreases correspondingly, as seen in Figure 11.

It can also be observed from Figure 10 that the PCM temperature difference between sections A and B is higher than the temperature difference between section B and section C. This is due to high heat transfer at section A, resulting in a sharp decrease in HTF temperature along the distance between section A and section B, followed by a gradual decrease in HTF after section B. The maximum temperature difference of PCM between sections A and B is 2.22°C, whereas the temperature difference between sections B and C is 1.23°C at t = 25 min. After t = 90 min, the axial temperature and liquid fraction variation become less significant. This is because, after t = 90 min, all PCM in the upper portion of the annulus is melted. Thus, the convection dominancy is diminished, see Figure 12, thereby reducing the heat transfer rate. As a rule of thumb, the lower heat transfer

between HTF and PCM causes more uniform temperature distribution along the axial direction for both HTF and heat transfer surfaces; see Figure 11. It can be concluded that the variation of PCM temperature and liquid fraction directly relates to the temperature distribution of HTF in a tube and outer shell. In other words, high heat transfers between PCM and HTF result in a high axial variation and vice versa.

Quantitatively, the total time required for complete melting is 151 min, 156 min, and 160 min for sections A, B, and C, respectively. This implies that the overall duration of melting for section B is extended by 3.31% compared to section A, while the total melting duration for section C is increased by 2.56% compared to section B.

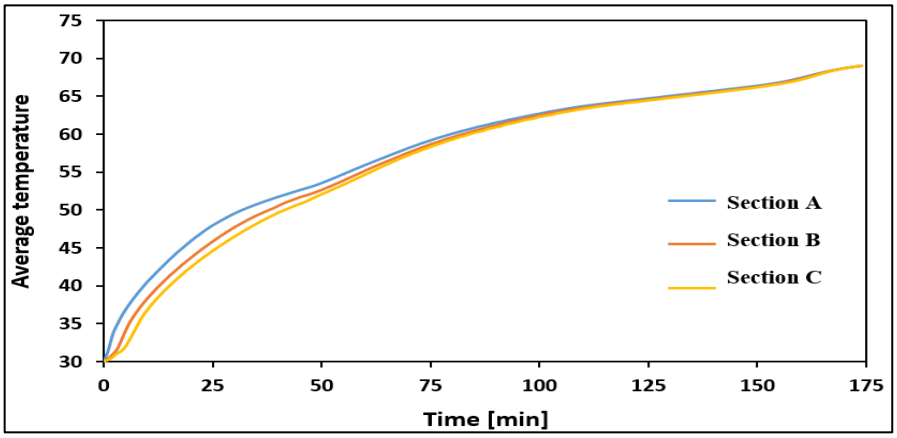

Figure 10: Average temperature versus time along the axial direction during charging proce

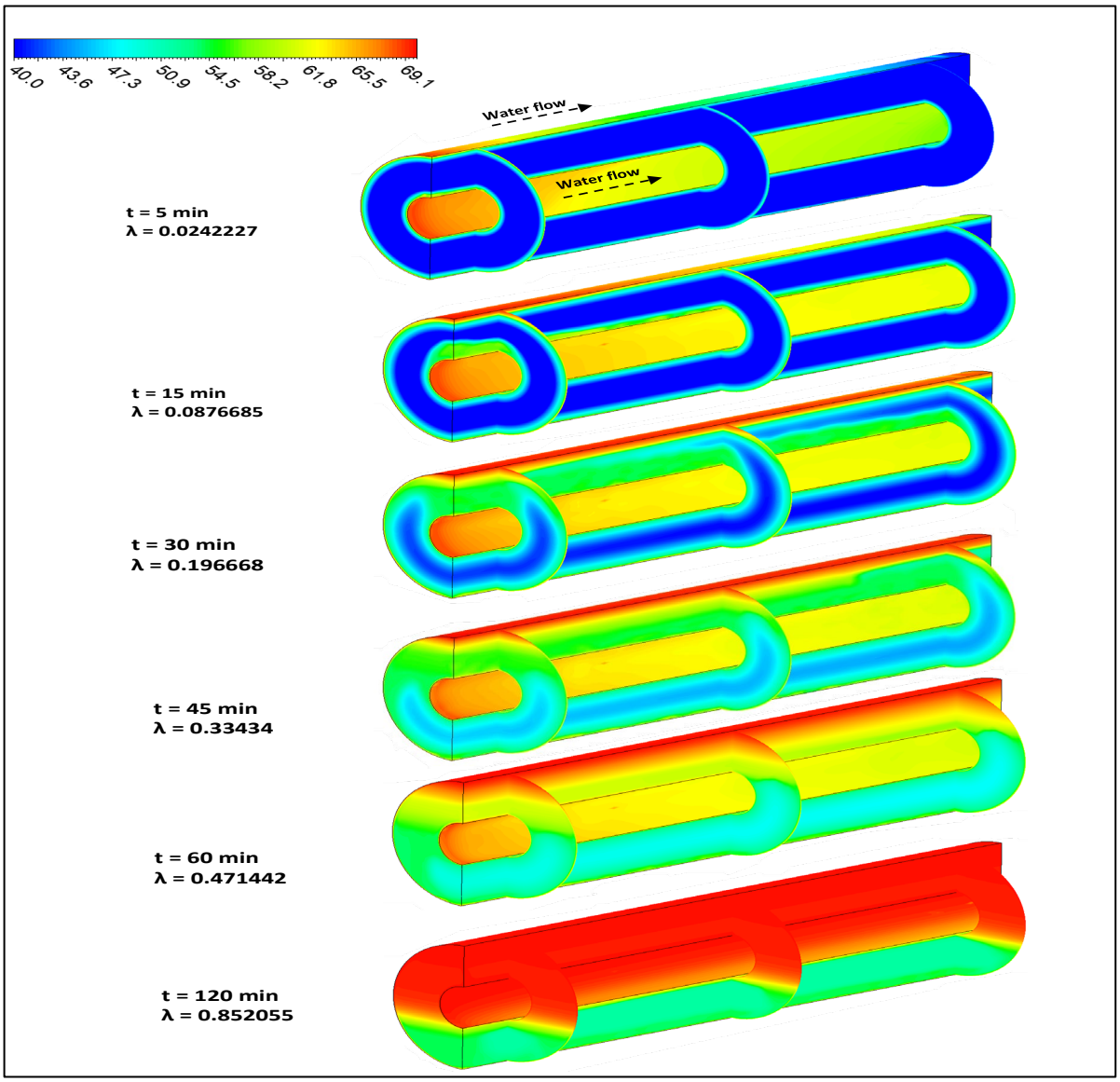

Figure 11: Temperature contour of 3-D model with time for $\dot{m}$ = 3 kg/min and HTFT = 70°C

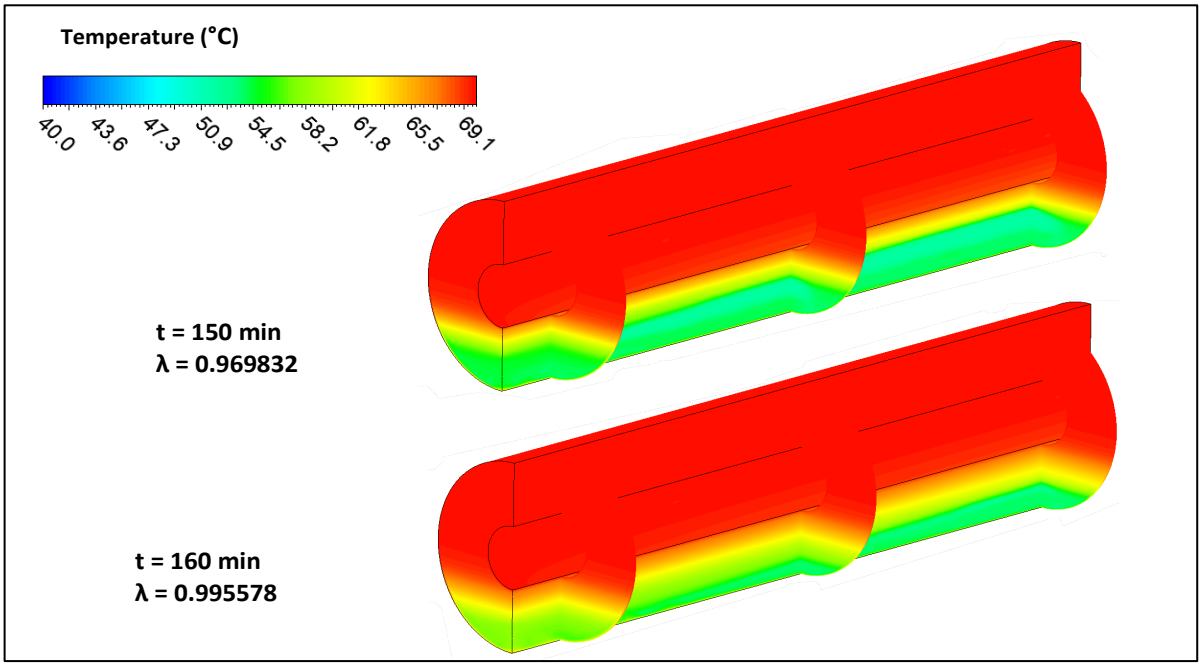

Figure 11: Continued

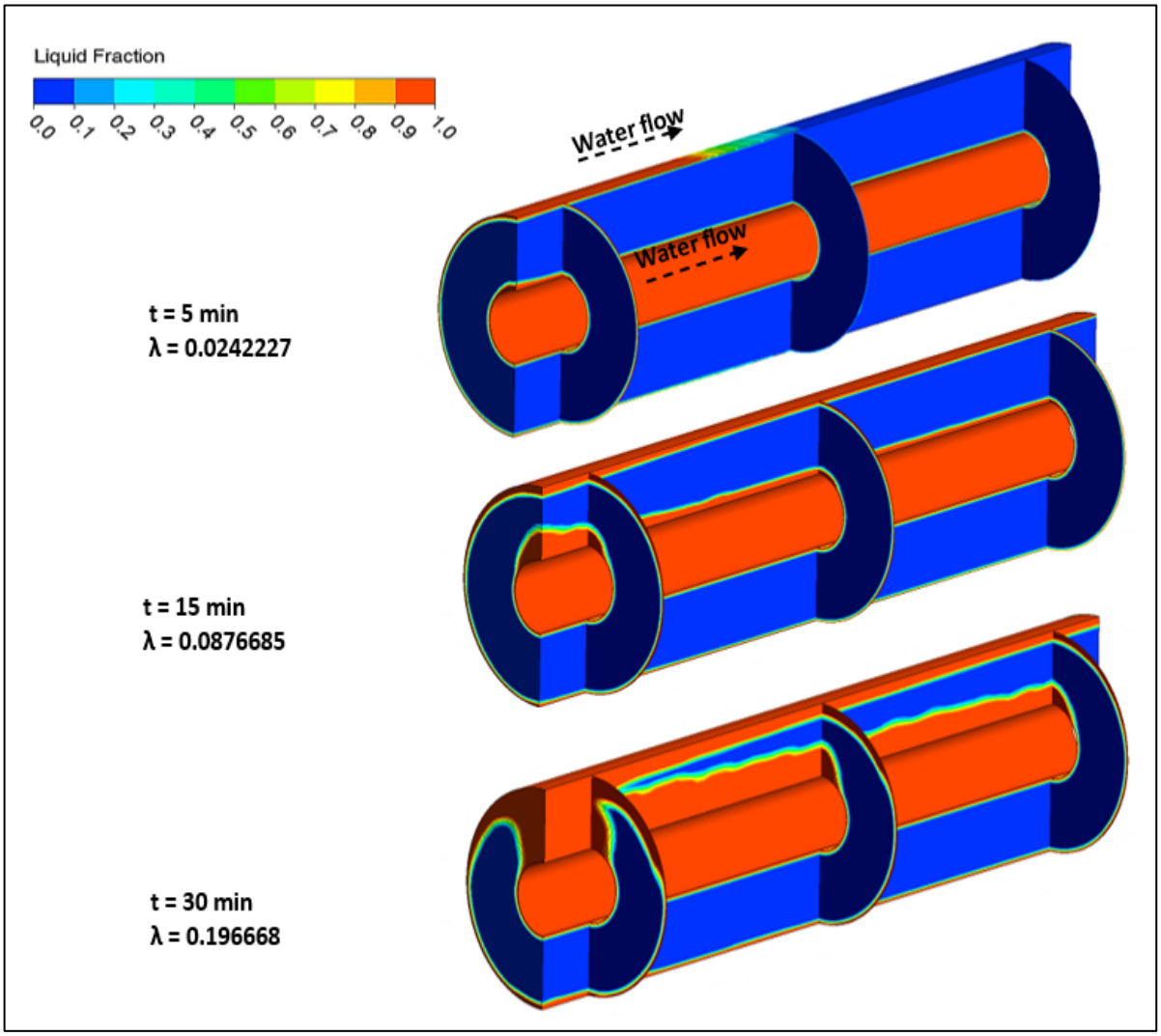

Figure 12: liquid fraction of 3-D model versus time at $\dot{m}$ = 3 kg/min and HTFT = 70°C

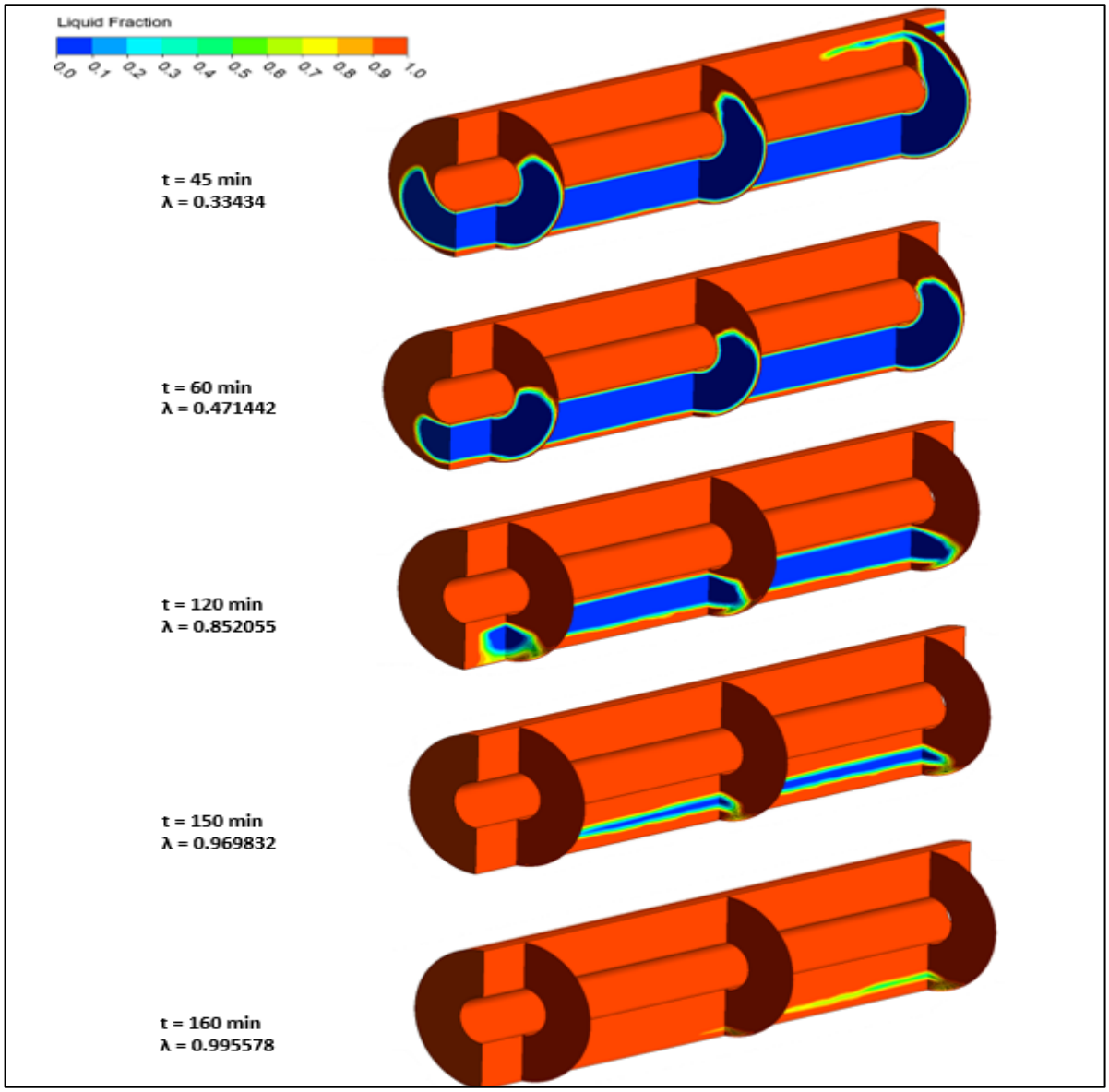

Figure 12: Continued

4.1.2 Angular variation

Figures 13 - 15 depicts the time-wise variation of average PCM temperature in the angular direction throughout the melting process for sections A, B, and C. These variations were predicted according to the average value of four thermocouples recordings located at the same angular direction (90°, 45°, 0°, -45°, and -90°). During the initial stage of charging (t = 10 min). Figure 13 shows the insignificant variation of the average PCM temperature over different angular directions, attributing to the efficient thermal diffusion and uniform heat conduction through the annulus in all directions. This condition is changed after t = 20 min as the average temperature at θ = 90° becomes higher than that at θ = -90° due to the creation of buoyancy force that pushes the hot melted PCM upward and thus speeds up the melting process in the upper part of annulus. However, the conduction heat transfer still dominates the lower part of the annulus. That is why the rate of temperature increase in the lower half is comparatively low. The average temperatures in the three angular directions θ = 90°, θ = 45°, and θ = 0° were almost identical at the end of the charging process. In contrast, the average temperature at θ = -45° and θ = -90° were lower. This difference can be ascribed to the effect of thermal diffusion and natural convection, as the PCM melting point was reached earlier in the angular directions θ = 90°, θ = 45°, and θ = 0° than in the other directions. Quantitatively, the time required to reach complete melting for angular directions θ = 90°, θ = 45°, θ = 0°, θ = -45° and θ = -90° are 33 min, 44 min, 69 min, 118 min, and 151 min, respectively. This means that the time required to complete melting in the lower Region (θ = -90°) is approximately 4.5 times the time required for the upper Region (θ = 90°).

Figure 14 and Figure 15 show the temperature change over time for sections B and C, respectively. A similar average temperature trend is observed for sections B and C compared to section A. However, Region I (sensible heat) of sections B and C takes longer than Section A. This is related to the temperature of heat transfer surfaces being lower for section B and C than section A, leading to decreased temperature difference between heat transfer surfaces and PCM, reducing the heat transfer rate. Therefore, the solid PCM takes longer to absorb the required sensible heat to reach melting point.

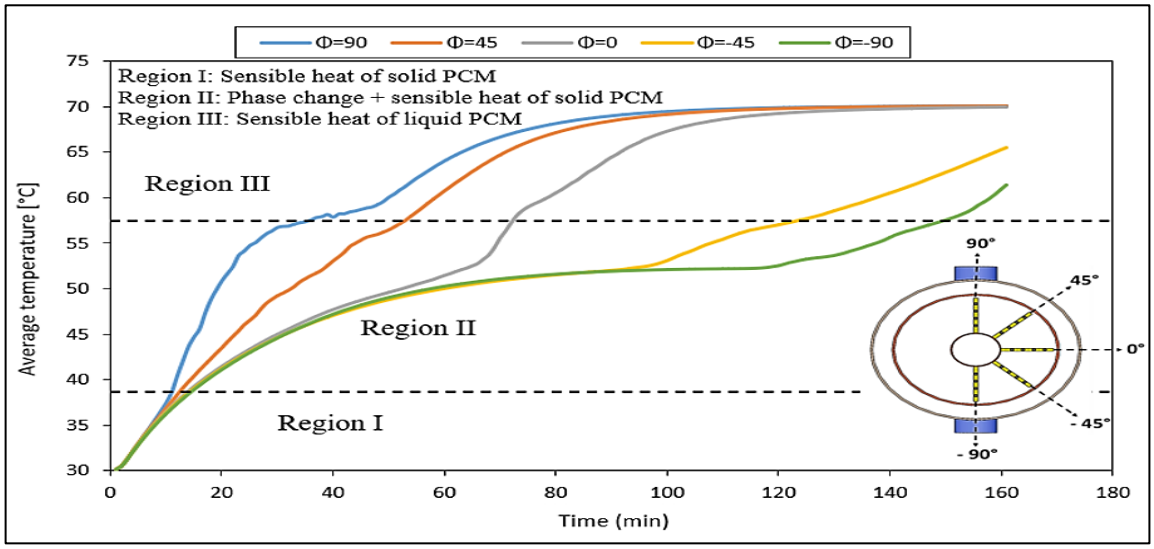

Figure 13: Average temperatures measured along the angular direction at Section A throughout the charging process

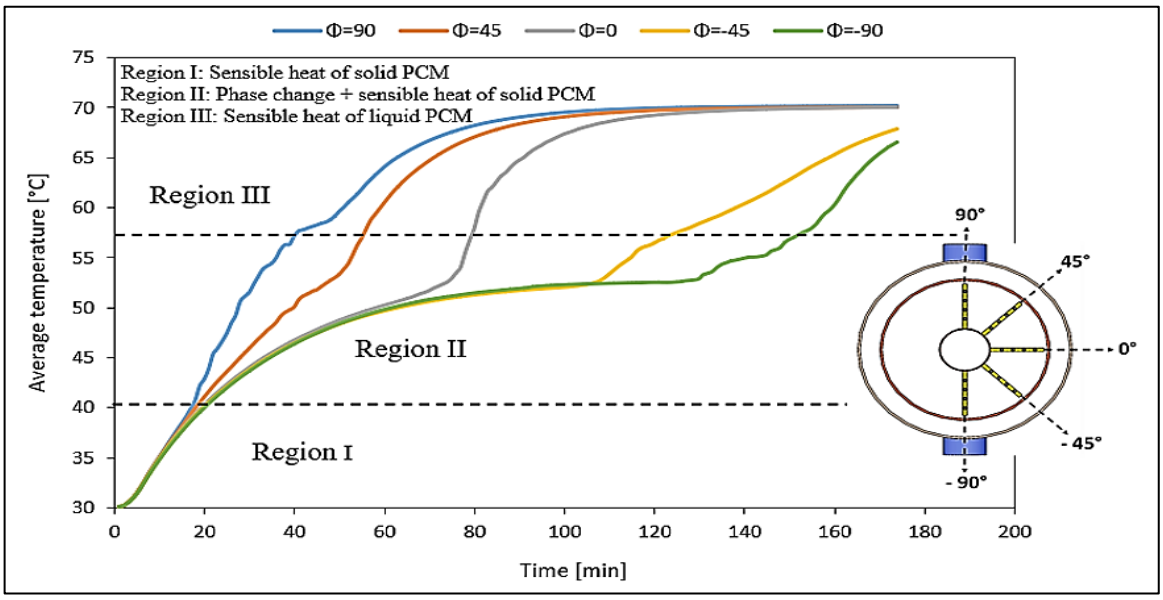

Figure 14: Average PCM temperature for different angular direction at section B during charging process

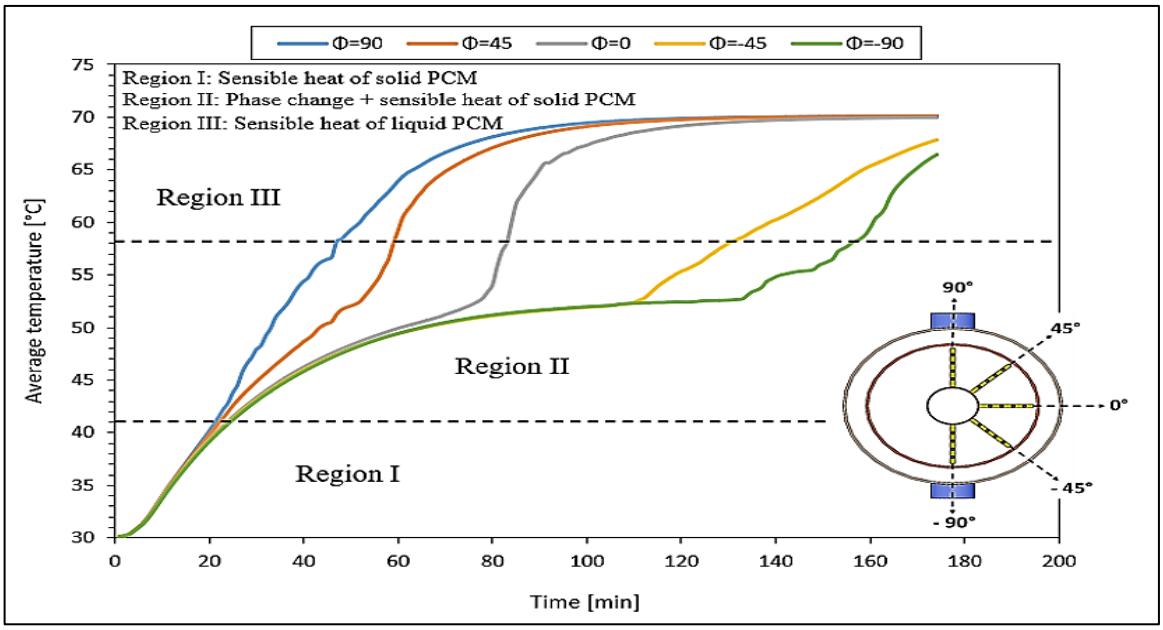

Figure 15: Average temperatures measured along the angular direction at Section C throughout the melting process

4.1.3 Radial variation

Figures 16-18 displays the average temperature of PCM along the radial axis at various periods of the melting process. These average temperature distributions were estimated by taking the average of five thermocouples at the same radial distance from the inner tube (r = 10, 20, 30, and 40 mm). At the initial stage of the charging process (t = 5 min), the temperature variations among the four distances were significantly observed. The temperature of the region (r = 40 mm) and region (r = 10 mm) are higher than other regions of PCM. This is because the Region (r = 40 mm) and Region (r = 10 mm) are respectively near to intermediate and inner heat transfer tubes directly in contact with hot water. However, there is an insignificant temperature change between r = 20 mm and r = 30 mm, away from heat transfer surfaces. It can be stated that the maximum temperature is noticed at a radial distance of 40 mm, with the second highest temperature occurring at a radial distance of 10 mm. This occurs due to the undue effect of the PCM's hot liquid the PCM's hot liquid phase towards the intermediate tube's upper region. In this Region, the liquid PCM absorbs a further amount of heat (referred to as sensible heat) from the surface, leading to a large increase in the average temperature of liquid PCM in region r = 40 mm.

As time passes, the temperature of zone r = 10 mm increases at a higher rate than other zones. After t = 120 min, the temperature of PCM at r = 10 mm becomes the highest, whereas it is the lowest temperature at r = 40 mm. This is because, after 120 minutes of melting, all PCM has melted except the region near the intermediate tube in the lower part of the annulus. Therefore, the liquid PCM absorbs heat from the inner tube as sensible heat, resulting in a sharp temperature increase of liquid PCM at r = 10 mm. However, a portion of the heat that transfers from the intermediate tube to liquid PCM is absorbed by solid PCM as latent heat, suppressing the temperature increase of region r = 40 mm.

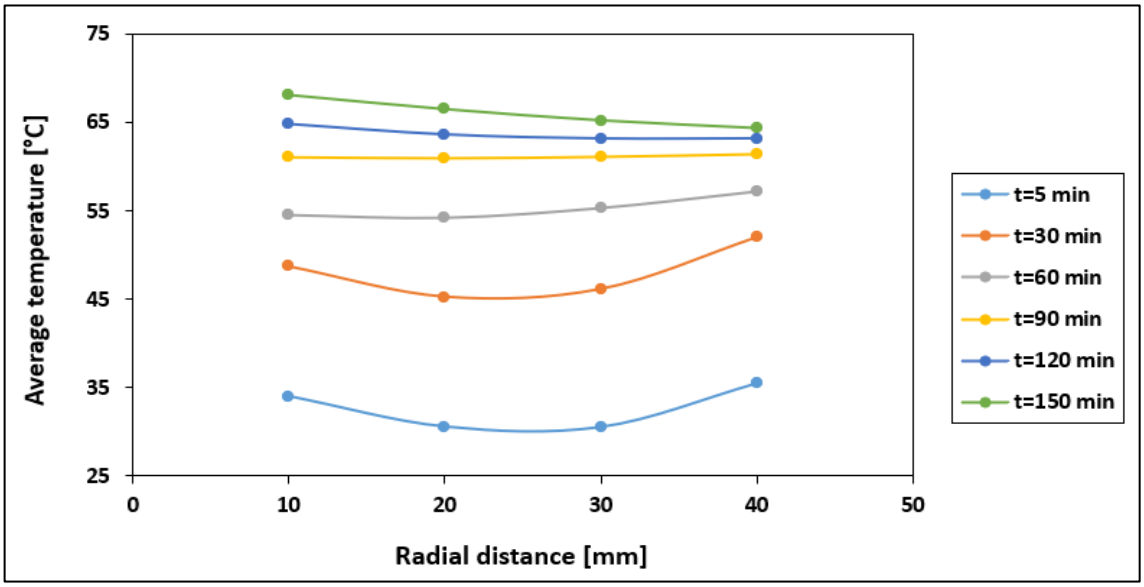

Figure 16: Average temperatures measured along the radial direction at Section A during the charging process

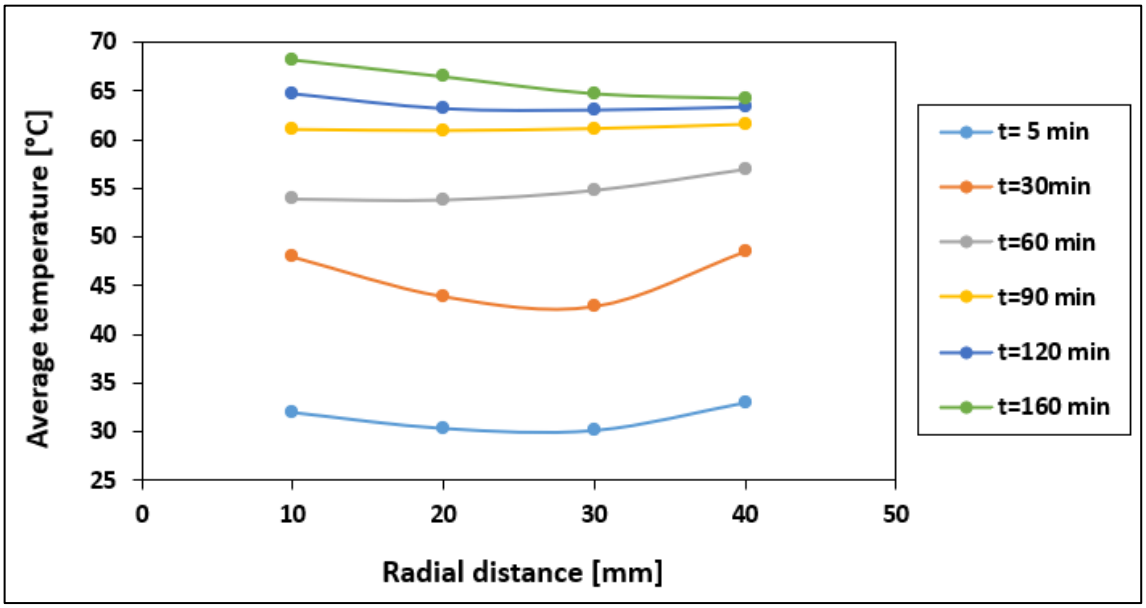

Figure 17: Average temperatures measured along the radial direction at Section B during the charging process

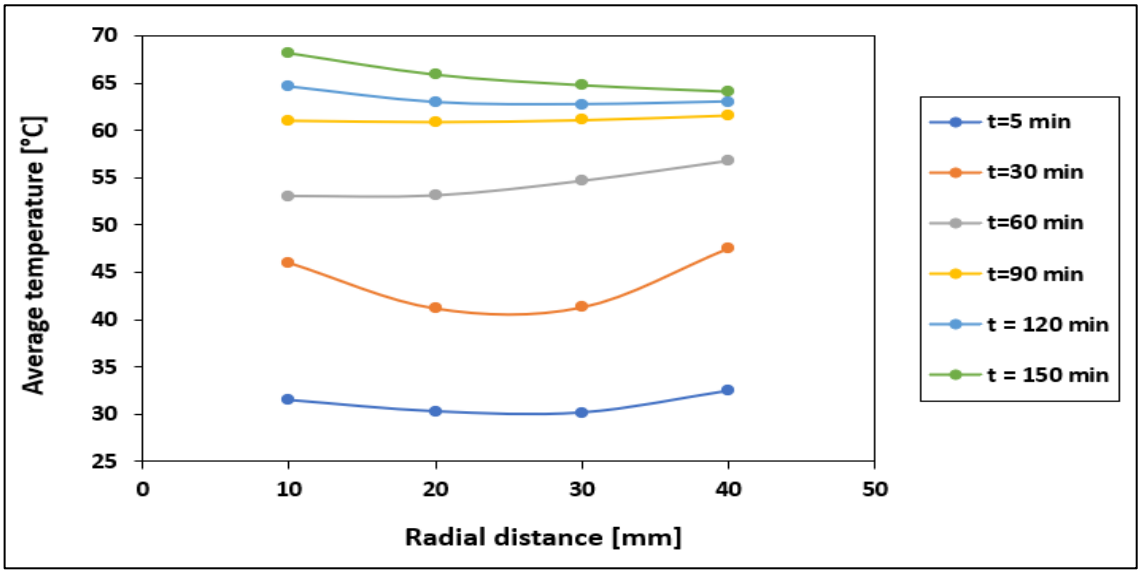

Figure 18: Average temperatures measured along the radial direction at Section C during the charging process

4.2 Microstructure of nanoparticles and composites

Figure 19 and Figure 20 illustrate the XRD patterns of Al_2O_3 and CuO nanoparticles, respectively. Based on Figure 19, various peak position to Υ-Al_2O_3 is exhibited in the XRD profile of Al_2O_3. The XRD trends of Al_2O_3 revealed three major peaks at 2θ angles of 36.2˚, 46.32˚, and 66.84˚. In addition, three distinct diffraction peaks at 2θ angles of 35.61˚, 38.84˚, and 48.87˚ are revealed in the XRD profile for CuO nanoparticles, see Figure 20. These strongest peak magnitudes were used to assess the crystallite size of the nanoparticles. Using Scherrer formulas, the average crystallite particle size of the Al_2O_3 and CuO were estimated to be 9.1 nm and 22.9 nm, respectively. The crystallite sizes of Al_2O_3 and CuO nanoparticles for each major peak are presented in Table 5.

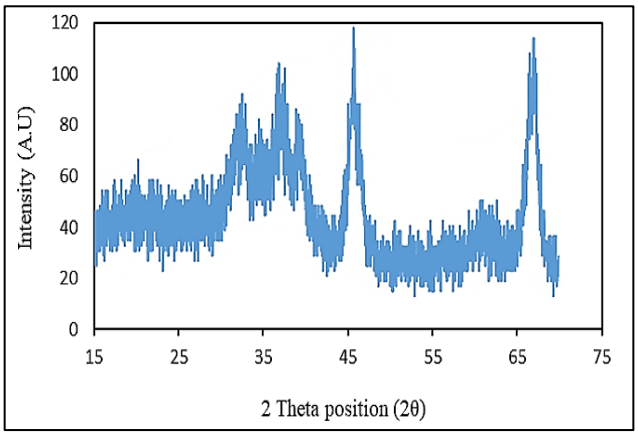

Figure 19: XRD profile of Al_2O_3 nanoparticles

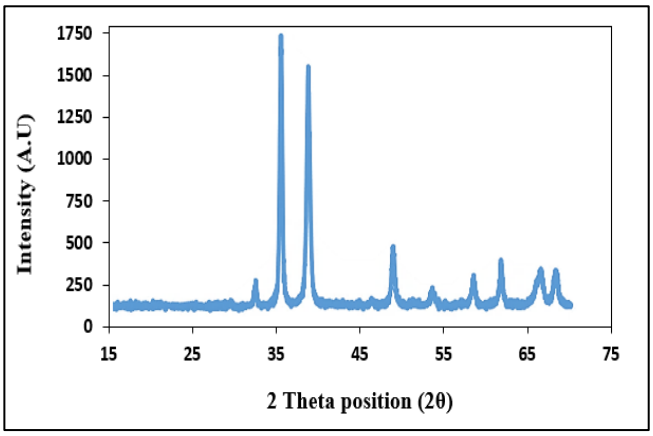

Figure 20: XRD profile of CuO nanoparticles

Table 5: Crystallite size of nanoparticle

substance	Peak position (2θ)	FWHM (β)	Crystallite size (nm)	Average size (nm)
Al_2O_3	36.2	0.8646	10.1	9.1
	46.32	0.96	9.4	
	66.8483	1.2433	8	
CuO	35.6158	0.338	25.79	22.9
	38.8421	0.4329	20.33	
	48.8793	0.4013	22.72	

Figures 21(A) and 21(B) demonstrate the transmission electron microscopy (TEM) image of Al_2O_3-CuO hybrid nano-PCM. The Al_2O_3 nanoparticles arrange themselves in a chain-like structure surrounding the CuO nanoparticles. This is because Al_2O_3 nanoparticles have a smaller particle size distribution than CuO nanoparticles. Furthermore, it can be noticed that both Al_2O_3 and CuO nanoparticles coexist in an agglomerated state and do not present as individual isolated structures. This proved that the Al_2O_3 and CuO nanoparticles interacted, which led to a wide range of particle sizes. It can also be observed that particles are almost spherical.

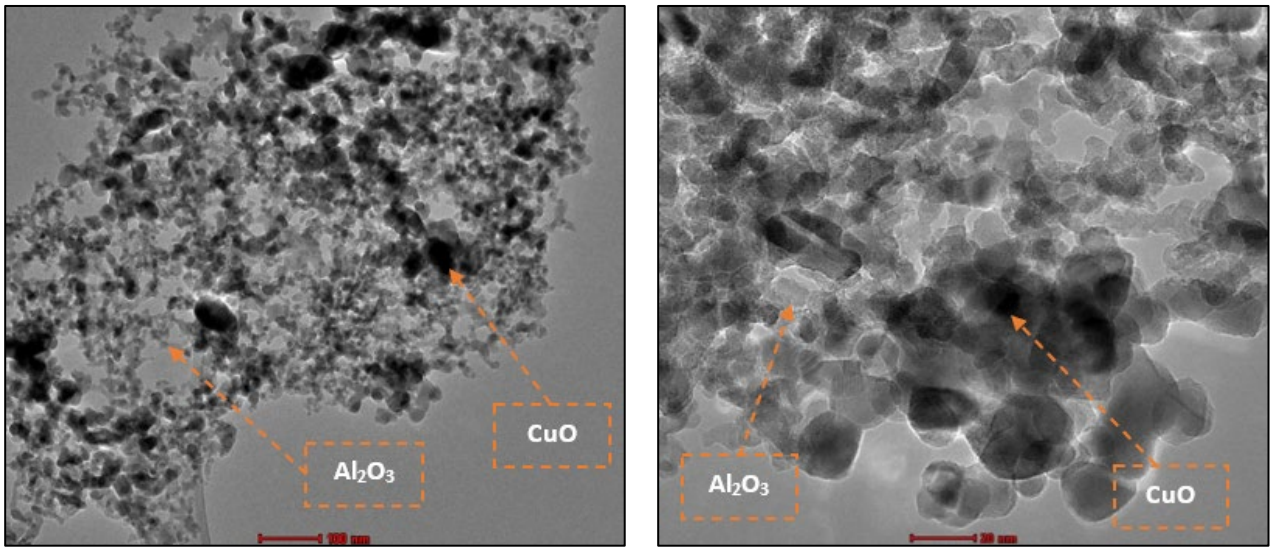

(A) **(B)**

Figure 21: TEM image of Al_2O_3-CuO hybrid nano-PCM (A) 100 nm and (B) 20 nm

4.3 Comparison between mono and hybrid nano-pcm

Figures 22 - 25 illustrate liquid fraction variation for various sorts of substances [Pure PCM, (CuO - PCM), (Al_2O_3 -PCM), and (50% CuO + 50% Al_2O_3 / PCM)] with different volume fractions (0.4, 0.8, 1.6 and 3.2%), respectively. Based on the figures, the liquid fraction of mono nanoparticles (CuO - PCM), (Al_2O_3 - PCM), and hybrid nano-PCM are higher than the pure PCM. However, the liquid fraction of hybrid Nano-PCM (CuO + Al_2O_3 - PCM) is higher than that of (Al_2O_3 - PCM) and (CuO - PCM) mono-Nano-PCM. This is because the thermal conductivity of hybrid nano-PCM is higher than mono-Nano-PCM's. It can be noticed from Figure 22 that the PCM with CuO has the lowest enhancement compared to PCM with Al_2O_3 and hybrid nano-PCM. This is due to the lowest increase in thermal conductivity and higher increase in mixture viscosity compared to Al_2O_3-PCM. As a rule of thumb, high viscosity resists the liquid movement. In comparison to pure PCM, the total melting time of hybrid Nano-PCM and Mono-Nano-PCM (Al_2O_3-PCM) and (CuO-PCM) for 0.4% concentration were reduced by 10.24, 9.03, and 3.01%, respectively.

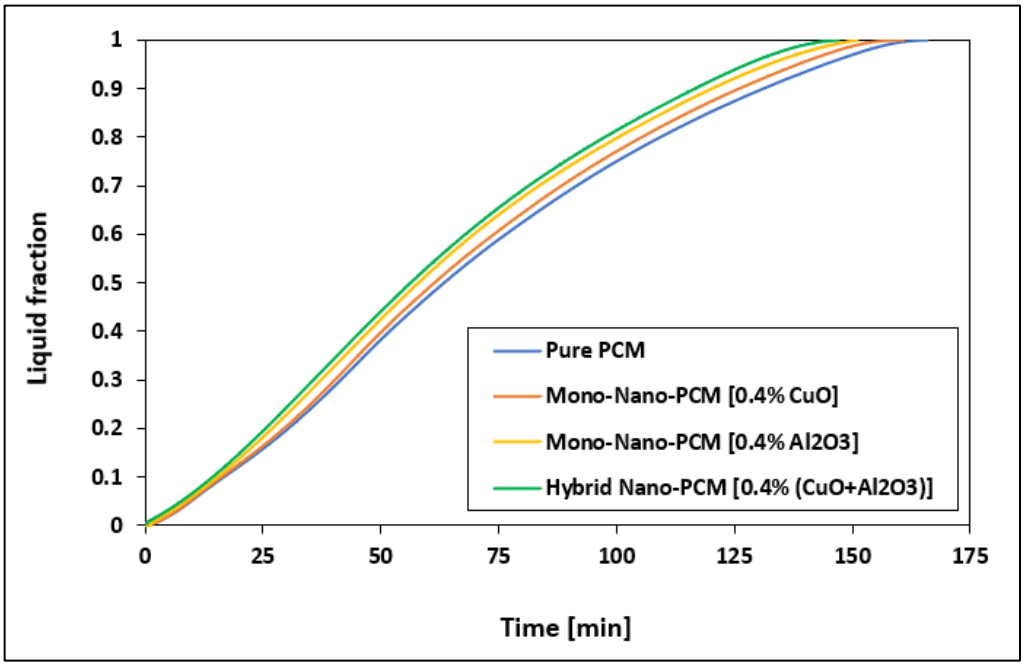

Figure 22: Liquid fraction of mono-nano-PCM and their hybrid at volume fraction of 0.4%

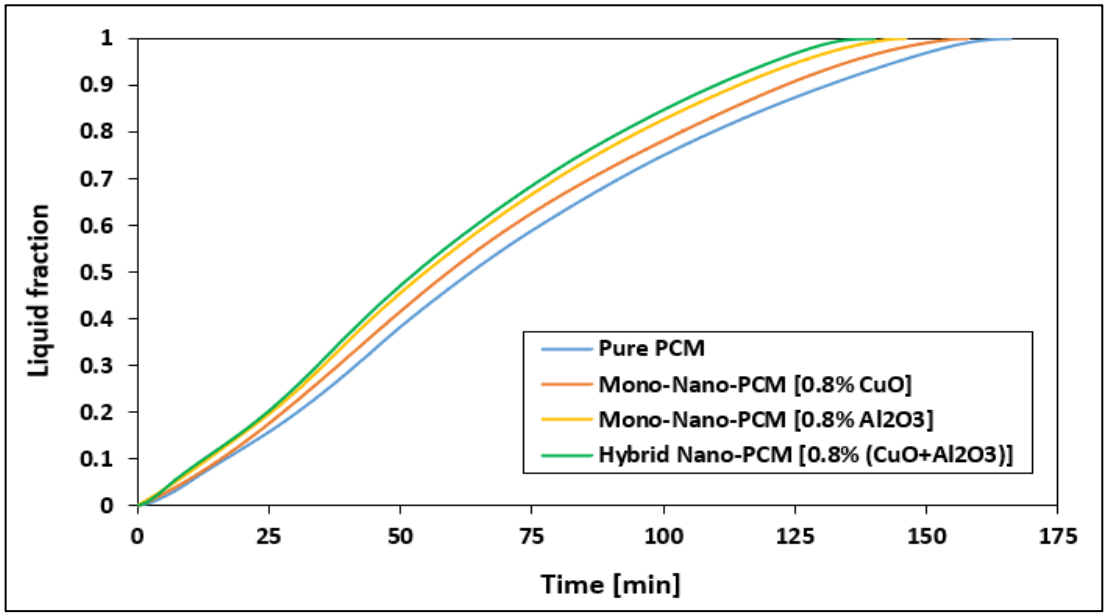

Figure 23: Comparison between liquid fraction of mono-nano-PCM and their hybrid at volume fraction of 0.8%

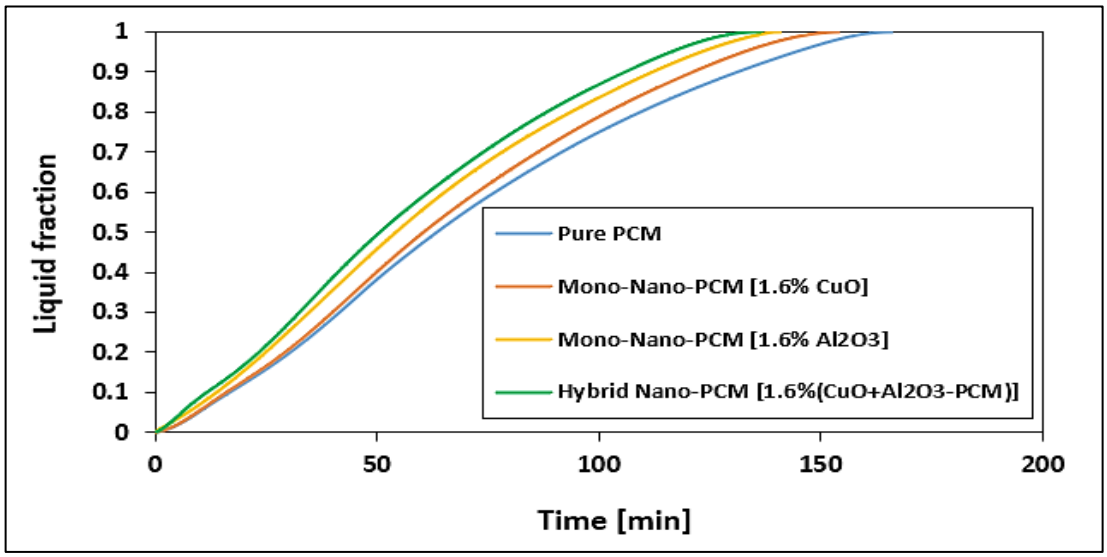

Figure 24: Comparison between liquid fraction of mono-nano-PCM and their hybrid at volume fraction of 1.6%

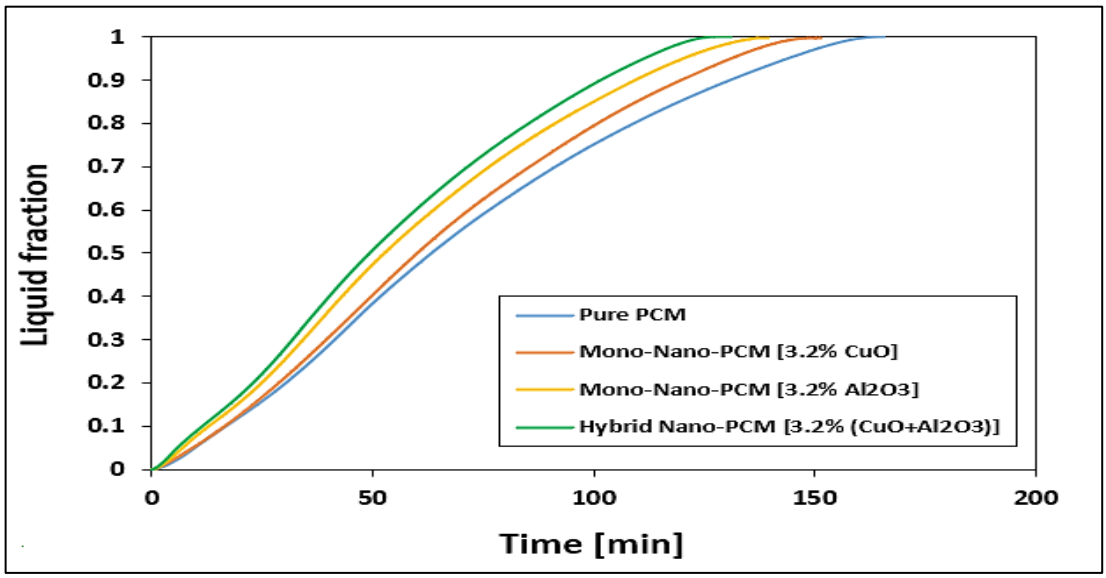

Figure 25: Liquid fraction of mono-nano-PCM and their hybrid at 3.2% volume fraction

Moreover, the total melting time of the hybrid Nano-PCM and mono-Nano-PCM (Al_2O_3-PCM) and (CuO-PCM) for 0.8% concentration were further reduced by 13.85, 12.04, and 4.81%, respectively compared to pure PCM, see Figure 23.

Figure 26 depicts the total melting time for pure PCM, mono-nano-PCM, and hybrid nano-PCM. Generally, the difference in total melting time between hybrid, Al_2O_3-PCM, and CuO-PCM increases with increasing the volume fraction and reaches its highest at 3.2% volume concentration. The total melting time decreased to 135 min, 138 min, and 152 min for the hybrid Nano-PCM, Al_2O_3-PCM, and CuO-PCM, respectively.

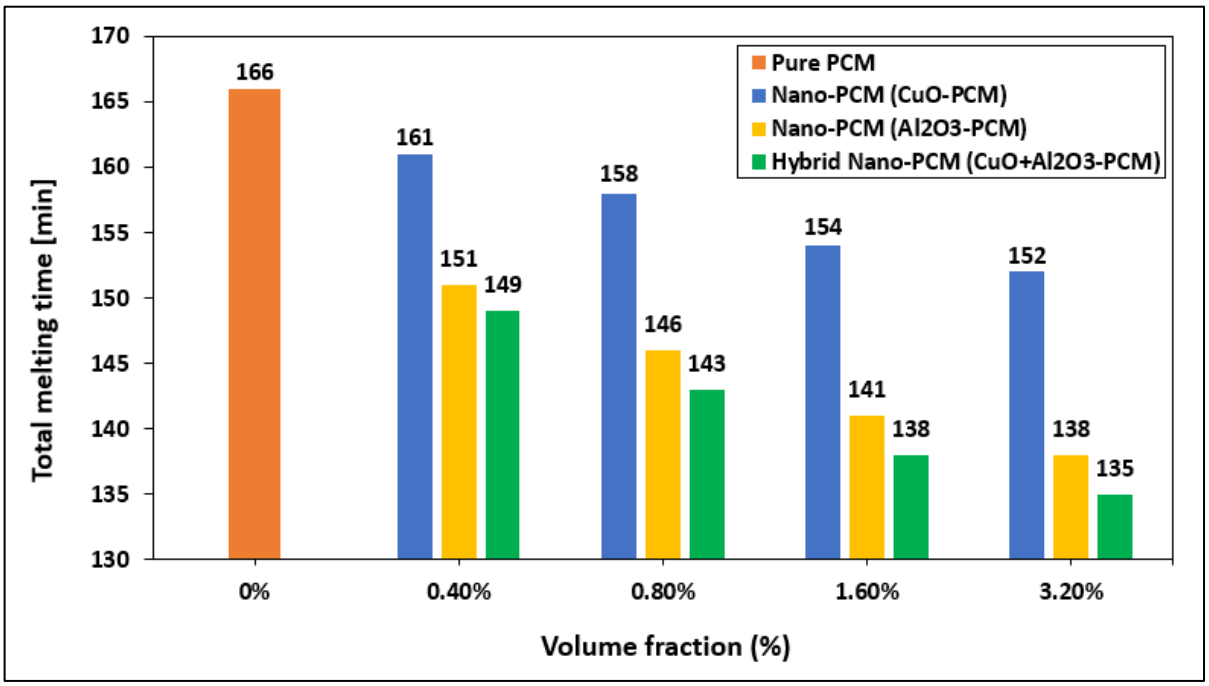

Figure 26: Total melting time for pure PCM, mono-nano-PCM and hybrid nano-PCM at various volume concentration

The stored energy at t = 90 min for different storage substances [Pure PCM, (CuO - PCM), (Al_2O_3 -PCM), and (50% CuO + 50% Al_2O_3 / PCM)] with various volume concentrations is presented in Figure 27. Regardless of Nano concentration, the stored energy for hybrid Nano-PCM is the highest, followed by Al_2O_3-PCM and CuO. This is because the hybrid Nano-PCM has the highest value of thermal conductivity and comparable value of latent heat of fusion, affecting the stored energy. Also, the hybrid Nano-PCM exhibits many interactions among its constituent nanoparticles.

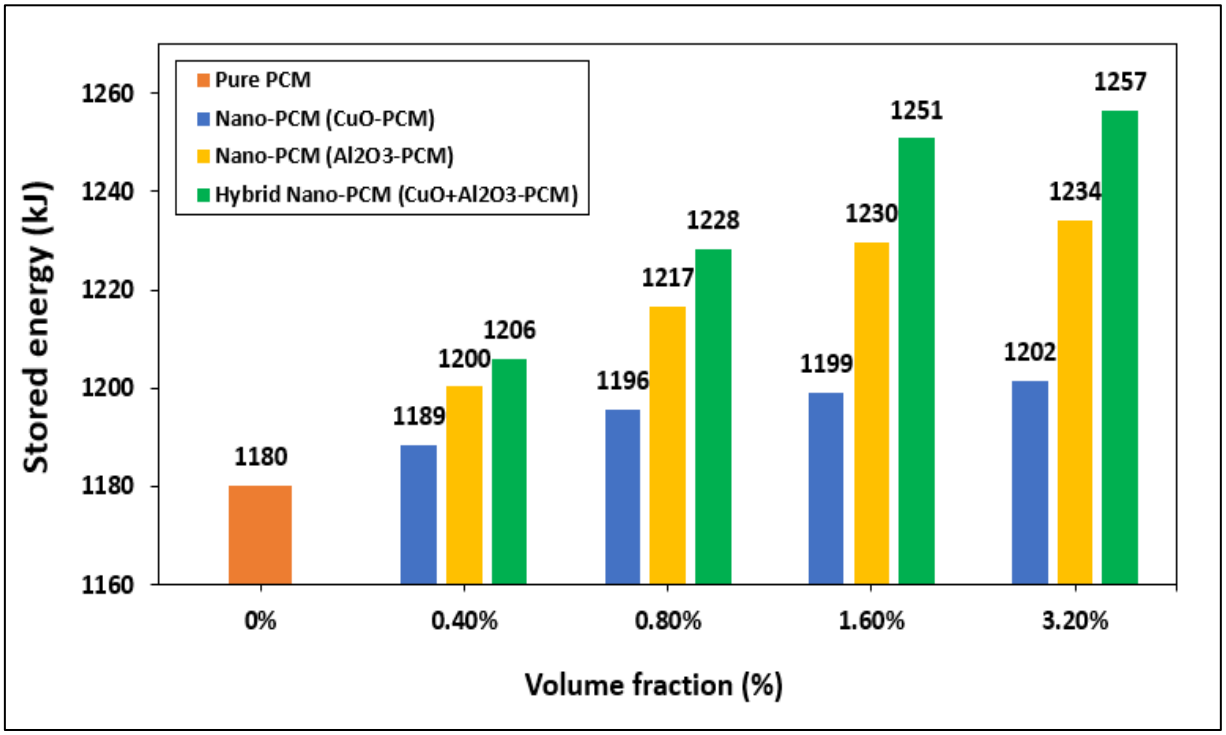

Figure 27: Stored energy for pure PCM, mono-nano-PCM and hybrid nano-PCM at various volume concentration

Furthermore, the stored energy of mono-Nano-PCM and hybrid Nano-PCM are increased with the volume fraction. However, there is an insignificant increase in the stored energy of CuO-PCM compared to pure PCM. This is because the CuO-PCM possesses the lowest thermal conductivity value and fusion latent heat. On the other hand, Al_2O_3-PCM has a moderate value of stored energy due to its comparable thermal conductivity value, the highest value of latent heat of fusion, and lower viscosity value. Increasing the stored energy with increasing volume fraction is related to the random movement of nanoparticles, which can flatten the temperature variation within the mixture and cause a sharp temperature change between the wall and the mixture. Consequently, the heat transfer between the wall and the mixture would be accelerated. Moreover, the micro-motion induced by nanoparticles augments the momentum exchange between liquid layers, increasing turbulence intensity and thus further amplifying the charging rate. In fact, the random micro-motion can be increased as the volume fraction of nanoparticles increases [58,59].

Table 6 shows the storage efficiency of mono-Nano-PCM and hybrid Nano-PCM. The storage efficiency can increase up to 77.15, 75.76, and 73.77% at a 3.2% volume fraction for hybrid nano-PCM, Al_2O_3-PCM, and CuO-PCM, respectively.

Table 6: Comparison of storage efficiency for different substances.

Volume fraction (%)	Substance	Melting time [min]	Reduction (%)	Stored energy (kJ)	Storage efficiency (%)
0	Pure PCM	166	-	1180.28	72.47
	CuO-PCM	161	3.01	1188.54	72.978
0.4	Al_2O_3-PCM	151	9.03	1200.34	73.7
	Hybrid nano-PCM	149	10.24	1206	74.05
	CuO-PCM	158	4.81	1195.62	73.41
0.8	Al_2O_3-PCM	146	12.04	1216.68	74.7
	Hybrid nano-PCM	143	13.85	1228.33	75.42
	CuO-PCM	154	7.22	1199.16	73.63
1.6	Al_2O_3-PCM	141	15.06	1229.67	75.5
	Hybrid nano-PCM	138	16.86	1250.78	76.8
	CuO-PCM	152	8.43	1201.52	73.77
3.2	Al_2O_3-PCM	138	16.86	1233.93	75.76
	Hybrid nano-PCM	135	18.67	1256.51	77.15

Based on the aforementioned argument, it can be concluded that the hybrid Nano-PCM is advantageous over mono-Nano-PCM in terms of heat transfer enhancement and energy recovery for all volume fractions, followed by mono-Nano-PCM (Al_2O_3 - PCM) and then CuO - PCM.

4.4 Correlations For Current Study

A novel correlation was proposed to predict liquid fraction, total melting time, and accumulative energy for hybrid nano-PCM.

The liquid fraction is correlated in terms of time volume fraction. Therefore, the liquid fraction is formulated in Equation 32:

$$\lambda = 1 - (1 - 0.00951 * t * \varphi^{0.07})^{1.47082} \quad (32)$$

The deviation between the evaluated result and the result estimated from the correlation above is illustrated in Figure 28A. As seen, the maximum discrepancy is ±7%.

The total melting time (τ) is correlated to volume fraction and HTFT in the Equation 33:

$$\tau = 43.0638 * \varphi^{-0.048} * \left(\frac{HTFT - T_m}{T_m}\right)^{-0.90894} \quad (33)$$

where, T_m is the meeting temperature of PCM. The maximum error between evaluated data and data obtained from Equation 33 does not exceed ± 4%, see Figure 28B.

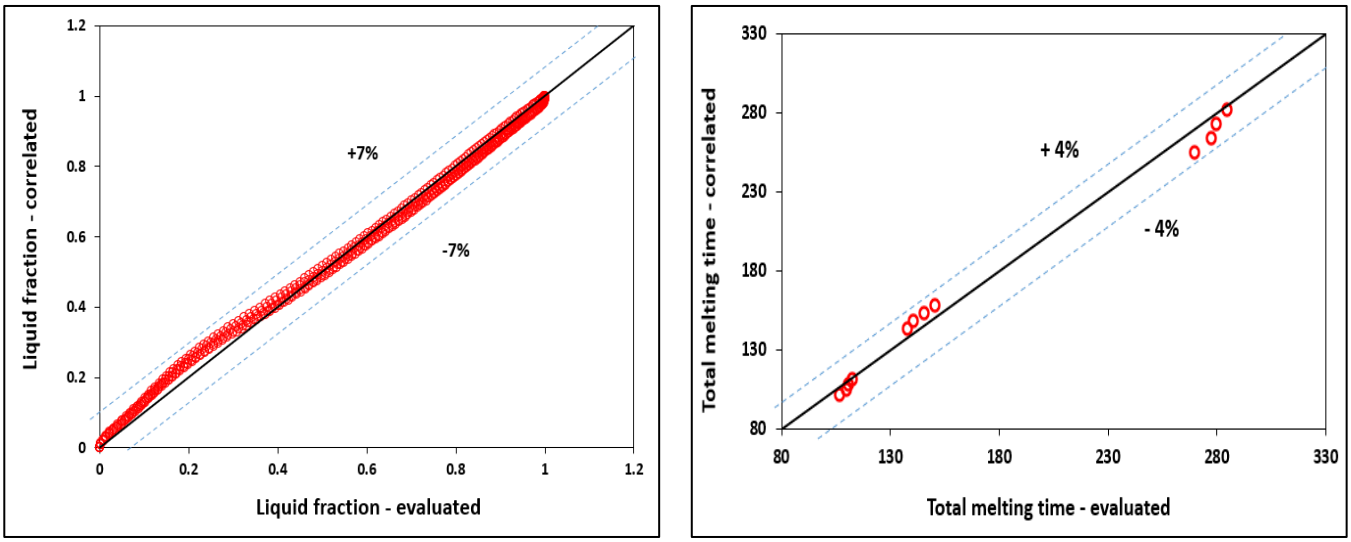

Figure 28: Comparison of evaluated and correlated result for melting process (A) liquid fraction (B) total melting time

5. Conclusion

The influence of using hybrid nano-PCM (Al_2O_3/CuO+PCM) on the thermal performance of a triplex tube heat storage (TTHS) was investigated and compared to those of the mono nano-PCM and pure PCM. The experiments and numerical analysis were conducted at various volume fractions of nanoparticles (0.4%, 0.8%, 1.6% and 3.2%). The upcoming major conclusions are obtained from this study:

- The hybrid Nano-PCM is superior to mono-Nano-PCM in terms of heat transfer enhancement and energy recovery for all volume fractions, followed by mono-Nano-PCM (Al_2O_3-PCM) and CuO-PCM.
- At 0.8% volume fraction, the hybrid Nano-PCM, mono-Nano-PCM (Al_2O_3-PCM), and CuO-PCM melted faster than pure PCM by 13.85%, 12.04%, and 4.81%, respectively.
- At 3.2% volume fraction, the storage efficiency can be improved and determined as 77.15, 75.76, and 73.77% for hybrid nano-PCM, Al_2O_3-PCM, and CuO-PCM, respectively.
- PCM with hybrid Nano-additive concentrations of 0.4%, 0.8%, 1.6%, and 3.2% can save the overall charging period by 10.2%, 13.8%, 16.8%, and 18.6%.
- By doubling the volume fraction from 1.6% to 3.2%, the accumulative energy was enhanced by only 5.73 kJ, and the storage efficiency was improved by only 0.35% for hybrid nano-PCM
- Correlations for time-based liquid fraction and total charging/discharging time are formulated to volume fraction. The maximum deviation between the evaluated result and predicted from correlations does not exceed ± 7% for liquid fraction and around ± 4% for total charging/discharging time.

Acknowledgment

This work was supported by the University of Technology, Ministry of Higher Education and Scientific Research, Baghdad, Iraq, and the self-determined research of authors.

Author contributions

Conceptualization, I. Sadiq, S. Aljabair and A. Karamallah; methodology, S. Aljabair and A. Karamallah; validation, I. Sadiq; formal analysis, S. Aljabair and A. Karamallah; investigation, I. Sadiq; data curation, I. Sadiq; writing—review and editing, I. Sadiq, A. Karamallah, and S. Aljabair and. All authors have read and agreed to the published version of the manuscript.

Funding

This research received no specific grant from any funding agency in the public, commercial, or not-for-profit sectors.

Data availability statement

The data that support the findings of this study are available on request from the corresponding author.

Conflicts of interest

The authors declare that there is no conflict of interest.

Nomenclature

Symbol	Definition	Units
$\vec{V}$	Fluid velocity	m/sec
P	Pressure	pa
$\vec{g}$	Gravity	m/sec2
T	Temperature	°C
$\vec{S}$	Darcy's law damping term	-
t	Time	Minute
h	sensible enthalpy	j/kg
ΔH	Latent heat content	j
Cp	Specific heat	J/kg °C
L	Latent heat of fusion	J/kg
k	Thermal conductivity	w/m °C

Greek symbols

ρ	Density	kg/m³
μ	Fluid viscosity	pa.s
β	Thermal expansion factor	1/K
λ	Liquid fraction	

Subscripts

56) Symbol	Description
npcm	Nano-phase change material
hnpcm	Hybrid nano phase change material
ref	Reference value
np1	Aluminum oxide nanoparticles
np2	Copper oxide nanoparticles
hnp	Hybrid nanoparticles
mush	Mushy

Abbreviations

Symbols	
	Fluid velocity (m/sec)
PCM	Phase change material
TTHS	Triplex tube heat storage
HTF	Heat transfer fluid
AlN	aluminium nitride
GNP	graphene nano-platelets
DSC	Differential scanning calorimetry

References

[1] A. Khudhair, F. Hatem, and D. Mohammed Ridha, Enhancement of Thermal Storage Properties of Phase Change Material by Using Metallic Swarf, J. Eng. Technol., 36 (2018) 586-595. https://doi.org/10.30684/etj.36.5A.15

[2] Akram H. Abed, Thermal Storage Efficiency Enhancement For Solar Air Heater Using a Combined Shsm and PCM Cylindrical Capsules System: Experimental Investigation, J. Eng. Technol., 34 (2016) 999-1011. https://doi.org/10.30684/etj.34.5A.16

[3] . Kalidasan, A. Pandey, S. Shahabuddin, M. Samykano, M. Thirugnanasambandam, and R. Saidur, Phase Change Materials Integrated Solar Thermal Energy Systems: Global Trends and Current Practices in Experimental Approaches, J. Energy Storage, 27 (2020) 101118. https://doi.org/10.1016/j.est.2019.101118

[4] Y. Fang, J. Niu, and S. Deng, Numerical analysis for maximizing effective energy storage capacity of thermal energy storage systems by enhancing heat transfer in PCM, Energy Build., 160 (2018) 10-18. https://doi.org/10.1016/j.enbuild.2017.12.006

[5] V. Safari, H. Abolghasemi, L. Darvishvand, and B. Kamkari, Thermal Performance Investigation Of Concentric And Eccentric Shell And Tube Heat Exchangers With Different Fin Configurations Containing Phase Change Material, J. Energy Storage, 37 (2021) 102458. https://doi.org/10.1016/j.est.2021.102458

[6] G. S. Sodhi and P. Muthukumar, Compound Charging and Discharging Enhancement in Multi-PCM System Using Non-Uniform Fin Distribution, Renew. Energy, 171 (2021) 299-314. https://doi.org/10.1016/j.renene.2021.02.084

[7] A. Ebrahimi, M. J. Hosseini, A. A. Ranjbar, M. Rahimi, and R. Bahrampoury, Melting Process Investigation Of Phase Change Materials in a Shell and Tube Heat Exchanger Enhanced With Heat Pipe, Renew. Energy, 138 (2019) 378-394. https://doi.org/10.1016/j.renene.2019.01.110

[8] Y.-Z. Ling, X.-S. Zhang, F. Wang, and X.-H. She, Performance Study Of Phase Change Materials Coupled With Three-Dimensional Oscillating Heat Pipes With Different Structures For Electronic Cooling, Renew. Energy, 154 (2020) 636-649. https://doi.org/10.1016/j.renene.2020.03.008

[9] Z. Haddad, F. Iachachene, M. A. Sheremet, and E. Abu-Nada, Numerical Investigation And Optimization Of Melting Performance For Thermal Energy Storage System Partially Filled With Metal Foam Layer: New Design Configurations, Appl. Therm. Eng., 223 (2023) 119809. https://doi.org/10.1016/j.applthermaleng.2022.119809

[10] G. Righetti, C. Zilio, G. A. Longo, K. Hooman, and S. Mancin, Experimental Study On The Effect Of Metal Foams Pore Size In A Phase Change Material Based Thermal Energy Storage Tube, Appl. Therm. Eng., 217 (2022) 119163. https://doi.org/10.1016/j.applthermaleng.2022.119163

[11] S. K. Singh, S. K. Verma, and R. Kumar, Thermal performance and behavior analysis of SiO_2, Al_2O_3 and MgO based nano-enhanced phase-changing materials, latent heat thermal energy storage system, J. Energy Storage, 48 (2022) 103977. https://doi.org/10.1016/j.est.2022.103977

[12] C. Nie, S. Deng, J. Liu, and Z. Rao, Performance Evaluation Of Shell-Tube Latent Heat Storage Unit Using Nanoparticles With Cascaded Concentration, J. Energy Storage, 62 (2023) 106892. https://doi.org/10.1016/j.est.2023.106892

[13] X. Yu and Y. Tao, Improvement of thermal cycle stability of paraffin/expanded graphite composite phase change materials and its application in thermal management, J. Energy Storage, 63 (2023) 107019. https://doi.org/10.1016/j.est.2023.107019

[14] X. Tang et al., Preparation and Application of Paraffin/Expanded Graphite-Based Phase Change Material Floor for Solar-Heat Pump Combined Radiant Heating Systems, Sustain. Chem. Eng., 11 (2023) 2871-2884. https://doi.org/10.1021/acssuschemeng.2c06289

[15] M. A. Fikri et al., Thermal Conductivity, Reliability, And Stability Assessment Of Phase Change Material (PCM) Doped With Functionalized Multi-Wall Carbon Nanotubes (FMWCNTs), J. Energy Storage, 50 (2022) 104676. https://doi.org/10.1016/j.est.2022.104676

[16] X. Li et al., Carbon nanotubes modified graphene hybrid Aerogel-based composite phase change materials for efficient thermal storage, Energy Build., 273 (2022) 112384. https://doi.org/10.1016/j.enbuild.2022.112384

[17] A. A. Al-Abidi, S. Mat, K. Sopian, M. Y. Sulaiman, and A. T. Mohammad, Internal And External Fin Heat Transfer Enhancement Technique For Latent Heat Thermal Energy Storage In Triplex Tube Heat Exchangers, Appl. Therm. Eng., 53 (2013) 147-156. https://doi.org/10.1016/j.applthermaleng.2013.01.011

[18] A. Shahsavar, A. Goodarzi, P. Talebizadehsardari, and M. Arıcı, Numerical Investigation Of A Double-Pipe Latent Heat Thermal Energy Storage With Sinusoidal Wavy Fins During Melting And Solidification, Int. J. Energy Res., 45 (2021) 20934-20948. https://doi.org/10.1002/er.7152

[19] M. Baou, F. Afsharpanah, and M. A. Delavar, Numerical Study Of Enhancing Vehicle Radiator Performance Using Different Porous Fin Configurations And Materials, Heat Transf. Res., 49 (2020) 502-518. https://doi.org/10.1002/htj.21624

[20] A. Liu, J. Lin, and Y. Zhuang, PIV Experimental Study On The Phase Change Behavior Of Phase Change Material With Partial Filling Of Metal Foam Inside A Cavity During Melting, Int. J. Heat. Mass. Transf.,187 (2022) 122567. https://doi.org/10.1016/j.ijheatmasstransfer.2022.122567

[21] M. Abbasi, S. M. Mousavi, B. J. Lee, J. A. Esfahani, N. Karimi, and M. Y. Mamaghani, Examination Of The Effects Of Porosity Upon Intensification Of Thermal Storage Of Pcms In A Shell-And-Tube Type System, Case Stud. Therm. Eng. 33 (2022) 101963. https://doi.org/10.1016/j.csite.2022.101963

[22] J. Du, R. Wang, Q. Zhuo, and W. Yuan, Heat Transfer Enhancement Of Fe3O4-Water Nanofluid By The Thermo-Magnetic Convection And Thermophorestic Effect, Int. J. Energy Res., 46 (2022) 9521-9532. https://doi.org/10.1002/er.7821

[23] W. Hamali and M. Y. Almusawa, Transient Heat Transfer Of NEPCM During Solidification Using Galerkin Method, Case Stud. Therm. Eng., 35 (2022) 102114, https://doi.org/10.1016/j.csite.2022.102114

[24] Y. A. Rothan, Thermal Analysis For Solidification Of PCM Including Nanoparticles Within A Container, Case Stud. Therm. Eng., 33 (2022) 101920. https://doi.org/10.1016/j.csite.2022.101920

[25] A. Chibani et al., A Strategy For Enhancing Heat Transfer In Phase Change Material-Based Latent Thermal Energy Storage Unit Via Nano-Oxides Addition: A Study Applied To A Shell-And-Tube Heat Exchanger, J. Environ. Chem. Eng., 9 (2021) 106744. https://doi.org/10.1016/j.jece.2021.106744

[26] C. Zhang, S. Han, Y. Wu, C. Zhang, and H. Guo, Investigation On Convection Heat Transfer Performance Of Quaternary Mixed Molten Salt Based Nanofluids In Smooth Tube, Int. J. Therm. Sci., 177 (2022) 107534. https://doi.org/10.1016/j.ijthermalsci.2022.107534

[27] M. Ghalambaz, A. Doostani, E. Izadpanahi, and A. Chamkha, Phase-Change Heat Transfer In A Cavity Heated From Below: The Effect Of Utilizing Single Or Hybrid Nanoparticles As Additives, J. Taiwan. Inst. Chem. Eng., 72 (2017) 104-115. https://doi.org/10.1016/j.jtice.2017.01.010

[28] M. Ghalambaz, S. M. H. Zadeh, S. Mehryan, I. Pop, and D. Wen, Analysis Of Melting Behavior Of Pcms In A Cavity Subject To A Non-Uniform Magnetic Field Using A Moving Grid Technique, Appl. Math. Model., 77 (2020) 1936-1953. https://doi.org/10.1016/j.apm.2019.09.015

[29] I. Sadiq, S. Aljabai, and A. Karamallah, Effect Of Al2O3/Cuo Hybrid Nanoparticles Dispersion On Melting Process Of PCM In A Triplex Tube Heat Storage, FME Transactions, 51 (2023) 606-626. https://doi.org/10.5937/fme2304606S

[30] F. Afsharpanah, M. Izadi, F. A. Hamedani, S. S. Mousavi Ajarostaghi, and W. Yaïci, Solidification of nano-enhanced PCM-porous composites in a cylindrical cold thermal energy storage enclosure, Case Stud. Therm. Eng., 39 (2022) 102421. https://doi.org/10.1016/j.csite.2022.102421.

[31] Arıcı, E. Tütüncü, Ç. Yıldız, and D. Li, Enhancement of PCM Melting Rate Via Internal Fin And Nanoparticles, Int. J. Heat Mass Transf., 156 (2020) 119845. https://doi.org/10.1016/j.ijheatmasstransfer.2020.119845

[32] N. H. Mohamed, F. S. Soliman, H. El Maghraby, and Y. M. Moustfa, Thermal Conductivity Enhancement Of Treated Petroleum Waxes, As Phase Change Material, By A Nano Alumina: Energy Storage, Renew. Sust. Energ. Rev., 70 (2017) 1052-1058. https://doi.org/10.1016/j.rser.2016.12.009

[33] P. M. Kumar, K. Mylsamy, K. Prakash, M. Nithish, and R. Anandkumar, Investigating Thermal Properties Of Nanoparticle Dispersed Paraffin (NDP) As Phase Change Material For Thermal Energy Storage, Mater. Today: Proc., 45 (2021) 745-750. https://doi.org/10.1016/j.matpr.2020.02.800

[34] M. Fathi and A. Hanifi, Evaluation And Characterization Of Nanostructure Hydroxyapatite Powder Prepared By Simple Sol–Gel Method, Mater. Lett., 61 (2007) 3978-3983. https://doi.org/10.1016/j.matlet.2007.01.028

[35] F. Agyenim, P. Eames, and M. Smyth, Experimental Study On The Melting And Solidification Behaviour Of A Medium Temperature Phase Change Storage Material (Erythritol) System Augmented With Fins To Power A Libr/H2O Absorption Cooling System, Renew. Energ., 36 (2011) 108-117. https://doi.org/10.1016/j.renene.2010.06.005

[36] M. J. Hosseini, M. Rahimi, and R. Bahrampoury, Experimental And Computational Evolution Of A Shell And Tube Heat Exchanger As A PCM Thermal Storage System, Int. Commun. Heat Mass Transf., 50 (2014) 128-136. https://doi.org/10.1016/j.icheatmasstransfer.2013.11.008

[37] R. J. Moffat, Describing The Uncertainties In Experimental Results, Exp. Therm. Fluid Sci., 1 (1988) 3-17. https://doi.org/10.1016/0894-1777(88)90043-X

[38] A. Brent, V. R. Voller, and K. Reid, Enthalpy-Porosity Technique For Modeling Convection-Diffusion Phase Change: Application To The Melting Of A Pure Metal, Numer. Heat Transf.; A: Appl., 13 (1988) 297-318. https://doi.org/10.1080/10407788808913615

[39] J. M. Mahdi and E. C. Nsofor, Solidification Of A PCM With Nanoparticles In Triplex-Tube Thermal Energy Storage System, Appl. Therm. Eng., 108 (2016) 596-604. https://doi.org/10.1016/j.applthermaleng.2016.07.130

[40] M. Sheikholeslami, Numerical Analysis Of Solar Energy Storage Within A Double Pipe Utilizing Nanoparticles For Expedition Of Melting, Sol. Energy Mater Sol. Cells, 245 (2022) 111856. https://doi.org/10.1016/j.solmat.2022.111856

[41] Z. Li, A. Shahsavar, A. A. A. A. Al-Rashed, and P. Talebizadehsardari, Effect Of Porous Medium And Nanoparticles Presences In A Counter-Current Triple-Tube Composite Porous/Nano-PCM System, Appl. Therm. Eng., 167 (2020) 114777. https://doi.org/10.1016/j.applthermaleng.2019.114777

[42] A. Mourad et al., The numerical analysis of the melting process in a modified shell-and-tube phase change material heat storage system, J. Energy Storage, 55 (2022) 105827. https://doi.org/10.1016/j.est.2022.105827

[43] E. Bellos and C. Tzivanidis, Thermal Analysis Of Parabolic Trough Collector Operating With Mono And Hybrid Nanofluids, Sustain. Energy Technol. Assess., 26 (2018) 105-115. https://doi.org/10.1016/j.seta.2017.10.005

[44] K. Khanafer and K. Vafai, A Critical Synthesis Of Thermophysical Characteristics Of Nanofluids, Int. J. Heat Mass Transf., 54 (2011) 4410-4428. https://doi.org/10.1016/j.ijheatmasstransfer.2011.04.048

[45] A. Sabah, Thermal and Hydrodynamic Characteristics of Hybrid Nano-Fluid Multiphase Flow in a Wavy Tube," Degree of Doctor of Philosophy, Mech. Eng. Dep., University of Technology, 2023.

[46] G. Batchelor, The Effect Of Brownian Motion On The Bulk Stress In A Suspension Of Spherical Particles, J. Fluid Mech., 83 (1977) 97-117. https://doi.org/10.1017/S0022112077001062

[47] M. Amani, P. Amani, A. Kasaeian, O. Mahian, and S. Wongwises, Thermal Conductivity Measurement Of Spinel-Type Ferrite Mnfe2o4 Nanofluids In The Presence Of A Uniform Magnetic Field, J. Mol. Liq., 230 (2017) 121-128. https://doi.org/10.1016/j.molliq.2016.12.013

[48] M. Al-Jethelah, S.H. Tasnim, S. Mahmud, Melting of nano-PCM in an enclosed space: Scale analysis and heatline tracking, Int. J. Heat Mass Transf., 119 (2018) 841-859. https://doi.org/10.1016/j.ijheatmasstransfer.2017.11.106

[49] A. V. Arasu and A. S. Mujumdar, Numerical study on melting of paraffin wax with Al2O3 in a square enclosure," Int. Commun. Heat Mass Transf., 39 (2012) 8-16. https://doi.org/10.1016/j.ijheatmasstransfer.2017.11.106

[50] A. O. Elsayed, Numerical Study On Performance Enhancement Of Solid–Solid Phase Change Materials By Using Multi-Nanoparticles Mixtures, J. Energy Storage, 4 (2015) 106-112. https://doi.org/10.1016/j.est.2015.09.008

[51] O. A. Alawi, N. A. C. Sidik, H. W. Xian, T. H. Kean, and S. N. Kazi, Thermal Conductivity And Viscosity Models Of Metallic Oxides Nanofluids, Int. J. Heat Mass Transf., 116 (2018) 1314-1325. https://doi.org/10.1016/j.ijheatmasstransfer.2017.09.133

[52] R. S. Vajjha and D. K. Das, Experimental Determination Of Thermal Conductivity Of Three Nanofluids And Development Of New Correlations, Int. J. Heat Mass Transf., 52 (2009) 4675-4682. https://doi.org/10.1016/j.ijheatmasstransfer.2009.06.027

[53] Israa Y. Daood, Effects of Nano-Fluids Types, Volume Fraction of Nano-Particles, and Aspect Ratios on Natural Convection Heat Transfer in Right-Angle Triangular Enclosure, J. Eng. Technol., 28 (2010) 5365-5388.

[54] S. Patankar, Numerical Heat Transfer And Fluid Flow, Washington, DC: Hemisphere, 1980, Google Scholar| Crossref.

[55] H. K. Versteeg and W. Malalasekera, An introduction to computational fluid dynamics: the finite volume method. Pearson education, 2007.

[56] V. Voller, A. Brent, and K. Reid, A Computational Modeling Framework for the Analysis of Metallurgical Solidification Process and Phenomena, Solidification Processing 1987, Third Int, in Conf., Sheffield, England, 1987.

[57] V. R. Voller and C. Prakash, A Fixed Grid Numerical Modelling Methodology For Convection-Diffusion Mushy Region Phase-Change Problems, Int. J. Heat Mass Transf., 30 (1987) 1709-1719. https://doi.org/10.1016/0017-9310(87)90317-6

[58] A. Albojamal, H. Hamzah, A. Haghighi, and K. Vafai, Analysis Of Nanofluid Transport Through A Wavy Channel, Numer. Heat Transf.; A: Appl., 72 (2017) 869-890. https://doi.org/10.1080/10407782.2017.1412679

[59] D. D. Vo et al., Effectiveness Of Various Shapes Of Al_2O_3 Nanoparticles On The MHD Convective Heat Transportation In Porous Medium: CVFEM Modelling, J. Therm. Anal. Calorim., 139 (2020) 1345-1353. https://doi.org/10.1007/s10973-019-08501-4